https://doi.org/10.5194/egusphere-2026-1469
Preprint. Discussion started: 23 April 2026

WRF simulations of stratospheric gravity waves from Typhoon Soudelor (2015): sensitivity to microphysics, cumulus parameterization, and boundary layer schemes

Yen-Sen Lu[1], Lars Hoffmann[1], Xue Wu[2,3], Corwin J. Wright[4], and Neil P. Hindley[4]
[1]Jülich Supercomputing Centre, Forschungszentrum Jülich, Jülich, Germany
[2]Laboratory of Middle Atmosphere and Global Environment Observation, Institute of Atmospheric Physics, Chinese Academy of Sciences, Beijing, China
[3]University of Chinese Academy of Sciences, Beijing, China
[4]Centre for Climate Adaptation and Environment Research, University of Bath, Bath, UK
Correspondence: Yen-Sen Lu (ye.lu@fz-juelich.de) and Lars Hoffmann (l.hoffmann@fz-juelich.de)

Abstract. Tropical cyclones are prominent sources of atmospheric gravity waves due to their intense and organized deep convection, yet the sensitivity of cyclone-induced gravity waves to model physics choices remains poorly constrained. Here, we examine how different physical parameterizations in the Weather Research and Forecasting (WRF) model influence the generation and characteristics of stratospheric gravity waves during the well-observed case of Typhoon Soudelor (2015). A suite of high-resolution simulations of the tropical cyclone employing multiple microphysics, planetary boundary layer, and cumulus parameterizations is analyzed. Gravity wave diagnostics are derived from vertical velocity variability and a localized S-transform spectral analysis. Although the simulations produce similar tropical cyclone tracks and intensities, they generate markedly different gravity wave responses. Differences in microphysics and boundary layer schemes lead to systematic variations in gravity wave amplitudes and spectral characteristics, while the inclusion of a cumulus parameterization consistently weakens deep convection and gravity wave amplitudes. These differences occur despite comparable background wind and stability conditions, demonstrating that gravity wave sensitivity is largely controlled by differences in diabatic forcing among the simulations. Our results highlight the critical role of model physics in shaping gravity wave generation and stratospheric wave characteristics and demonstrate the importance of carefully evaluating diabatic forcing in mesoscale modeling studies.

1 Introduction

Tropical cyclones (TCs), referred to as typhoons in the western North Pacific, are among the most destructive natural hazards, characterized by intense winds and heavy precipitation (Emanuel, 2005; Peduzzi et al., 2012; Knutson et al., 2020). Forming over warm tropical and subtropical oceans, these low-pressure systems can develop into powerful storms that cause severe damage to human society and natural environments. The associated strong winds and extreme rainfall damage infrastructure, disrupt transportation, induce flooding in populated areas, and are a primary trigger of landslides in mountainous regions (Wu and Kuo, 1999; Huang and Wang, 2015).

https://doi.org/10.5194/egusphere-2026-1469
Preprint. Discussion started: 23 April 2026

In addition to their societal impacts, TCs play an important role in atmospheric dynamics. As highly organized deep convective systems, they are efficient sources of atmospheric gravity waves. Strong updrafts and downdrafts, together with intense latent heat release within the storm core, act as primary forcing mechanisms for gravity wave generation (Alexander et al., 1995; Lane et al., 2001; Beres et al., 2002; Kim et al., 2007; Kim and Chun, 2010). These gravity waves propagate upward from the troposphere into the stratosphere and mesosphere, transporting energy and momentum, modulating temperature variability, and influencing the circulation and distribution of atmospheric constituents. Through this process, TCs provide an important pathway for vertical coupling between the lower and upper atmosphere.

Accurate numerical simulation of TCs remains a major challenge due to the complex interactions among atmospheric dynamics, physical parameterizations, and microphysical processes (Krishnamurti et al., 2010; Islam and Takagi, 2020; Shirai et al., 2022). Additional difficulties arise from uncertainties in initial conditions and data assimilation, as well as from computational constraints that limit spatial resolution and ensemble size, as often found in general Earth system and high-resolution numerical weather prediction studies (Satoh et al., 2019; Gettelman et al., 2022). These limitations also directly affect the fidelity of TC simulations. Despite substantial progress over recent decades (DeMaria et al., 2014; Emanuel and Zhang, 2016; Chen et al., 2019), operational forecast errors remain non-negligible. For example, an analysis of National Hurricane Center forecasts in the Atlantic basin from 1990 to 2019 reported a mean track error of approximately $50\,\mathrm{km}$ at a 24-hour lead time, even in the most recent decade, reflecting persistent limitations in predictability and model performance (Cangialosi et al., 2020). High-resolution modeling and improved representations of physical processes are therefore essential for advancing TC prediction and understanding TC-related phenomena.

Because of their multiscale structure and strong diabatic forcing, TCs place particularly stringent demands on model physics. Simulated TC intensity, structure, and evolution are known to be sensitive to choices of microphysics, cumulus parameterization, and planetary boundary layer (PBL) schemes, as well as to numerical methods and initial conditions (Yang and Lin, 2005; Davis et al., 2008; Nolan et al., 2009; Gentry and Lackmann, 2010; Chu et al., 2011; Tao et al., 2011; Shirai et al., 2022). While many studies have examined how these choices affect TC track and intensity, less attention has been paid to their impacts on the simulated gravity waves generated by TCs and their subsequent propagation into the stratosphere. This represents an important gap, as gravity wave characteristics depend strongly on the vertical distribution, temporal variability, and intensity of latent heating, all of which are directly controlled by model physics.

In this study, we investigate how different physics parameterizations in a regional atmospheric model influence both TC simulations and the resulting stratospheric gravity wave response. For the simulations, we employ the Weather Research and Forecasting (WRF) model (Skamarock and Klemp, 2008), developed by the National Center for Atmospheric Research (NCAR) and the National Oceanic and Atmospheric Administration (NOAA). The WRF Advanced Research Weather (WRF-ARW) core is widely used for high-resolution TC simulations due to its ability to resolve atmospheric dynamics at fine temporal and spatial scales. Previous studies have demonstrated its skill in simulating TC intensity, structure, and evolution (Choudhury and Das, 2017; Cangialosi et al., 2020; Shirai et al., 2022), as well as TC-induced gravity waves (Wu et al., 2022, 2025).

We focus on Typhoon Soudelor (2015), an intense and well-observed tropical cyclone in the western North Pacific, which provides a well-suited case for examining TC-induced gravity wave generation. Soudelor was observed from 29 July to 12

August 2015 and reached Category 5 intensity at 1800 UTC on 3 August, with maximum wind speeds of up to $59.16\,\mathrm{m\,s^{-1}}$ (JMA, 2016; Fakour et al., 2016). The storm made landfall in Taiwan on 8 August, causing widespread flooding, landslides, power outages affecting approximately 4.5 million households, and substantial agricultural losses. Soudelor is regarded as the most intense typhoon of the 2015 typhoon season (Wang et al., 2023) and thus represents a well-suited case for studying the interaction between the storm's extreme convection and gravity wave generation.

The primary objective of this study is to assess the sensitivity of the simulated TC and its associated stratospheric gravity waves to different model physics choices. By investigating one well-studied storm in detail, we are able to study more combinations of physics options and benefit from the context provided by previous studies, with particular emphasis on microphysics, planetary boundary layer schemes, and cumulus parameterization. While different physics configurations may produce similar TC tracks and intensities within observational uncertainty, we hypothesize that they lead to systematically different latent heating structures, which in turn strongly affect the amplitude, vertical propagation, and spectral characteristics of stratospheric gravity waves. Using a well-observed tropical cyclone as a controlled test case, this study is designed as a process-oriented investigation aimed at isolating the physical mechanisms governing gravity wave generation and vertical coupling.

This paper is organized as follows. Section 2 describes the numerical model configuration, physics parameterizations, and observational datasets used for the assessment. Section 3 presents the simulated TC characteristics and gravity wave responses under different physics configurations. The implications of these findings are discussed in Section 4, and the main conclusions are summarized in Section 5.

2 Data and methods

2.1 Tropical cyclone track and intensity data

Best-track data of Typhoon Soudelor from the International Best Track Archive for Climate Stewardship (IBTrACS; Knapp et al. (2010)) are used to evaluate the simulation results. The IBTrACS dataset provides three-hourly estimates of storm position, maximum sustained wind speed (MSW), and minimum sea-level pressure (MSLP), which are compared with the simulated typhoon track and intensity. In the simulations, the typhoon center is identified using a simple algorithm that locates the grid point with the minimum sea-level pressure within the model domain. This approach enables a consistent comparison of storm paths and intensity evolution between observations and model outputs.

2.2 Satellite observations of clouds and gravity waves

Observations of clouds and stratospheric gravity waves associated with Typhoon Soudelor were obtained from the Atmospheric Infrared Sounder (AIRS) aboard NASA's Aqua satellite (Aumann et al., 2003; Chahine et al., 2006). Aqua is a sun-synchronous polar-orbiting satellite at an altitude of $705\,\mathrm{km}$, with equatorial crossing times of 13:30 and 01:30 local time (LT) at the ascending and descending nodes, respectively. AIRS is a hyperspectral infrared sounder that provides $2{,}378\,\mathrm{channels}$ spanning wavelengths from 3.74 to $15.40\,\mu\mathrm{m}$, with a horizontal footprint of approximately $13.5\,\mathrm{km}$ at nadir and near-global coverage twice daily.

Following Hoffmann et al. (2013, 2014), the presence of stratospheric gravity waves was identified through analysis of brightness temperature perturbations averaged over 42 AIRS channels within the $4.3\,\mu\mathrm{m}$ CO_2 absorption band, with weighting functions peaking between 30 and $40\,\mathrm{km}$ altitude. These channels, which target the carbon dioxide ν_3 fundamental band, exhibit strong sensitivity to stratospheric temperature while being insensitive to tropospheric clouds and water vapor. Due to the nadir sounding geometry, AIRS observations are particularly sensitive to gravity waves with long vertical wavelengths ($\lambda_z \geq 15\,\mathrm{km}$) and short horizontal wavelengths ($30\,\mathrm{km} \leq \lambda_x \leq 1{,}000\,\mathrm{km}$). AIRS measurements in atmospheric window regions facilitate simultaneous observations of clouds, allowing identification of potential convective sources of gravity wave events. The presence of high cloud tops, indicative of convective activity, is identified using an $8.1\,\mu\mathrm{m}$ atmospheric window channel, in which low brightness temperatures correspond to cold cloud tops.

For cloud observations with improved temporal coverage compared to AIRS, outgoing longwave radiation (OLR) data were obtained from the Stretched Visible and Infrared Spin Scan Radiometer (S-VISSR) installed on the FengYun-2G satellite (Xian et al., 2021). The FengYun-2G satellite, operated by the National Satellite Meteorological Center (NSMC) of the China Meteorological Administration (CMA), is a geostationary satellite with a sub-satellite point located at $104.5°\mathrm{E}$ over the equator. The satellite was launched on 31 December 2014 and has provided continuous data since 3 June 2015. The OLR product is retrieved from the $10.3\,\mu\mathrm{m}$ to $11.3\,\mu\mathrm{m}$ infrared window channel (IR1) and is available as a Level-2 product with three-hourly temporal resolution and a horizontal resolution of $10\,\mathrm{km}$. For consistency with cloud-top temperature diagnostics, we converted the radiance-based OLR measurements to equivalent brightness temperatures using the inverse Planck function.

2.3 WRF model and simulation setup

The Advanced Research WRF core (WRF-ARW), version 4.4.1, was used to simulate Typhoon Soudelor from 00:00 UTC on 6 August 2015 to 00:00 UTC on 9 August 2015, yielding a total simulation period of 72 hours. Model output is saved at 15-minute intervals for most variables, with higher-frequency output (6-minute intervals) for wind and temperature fields. The initial and lateral boundary conditions are derived from the European Centre for Medium-Range Weather Forecasts (ECMWF) ERA5 reanalysis dataset, which provides global atmospheric fields at hourly temporal resolution (Hersbach et al., 2020). Land-use and soil information are taken from the default WRF static input datasets, which are primarily based on MODIS observations.

The model domains use a Lambert conformal map projection, with the outer domain, referred to as Domain 01, centered at (25.0°N, 140.0°E). A moving nested domain, referred to as Domain 02, is employed to follow the evolution of the typhoon, guided by the storm track obtained from the IBTrACS database. The horizontal grid spacings are $15\,\mathrm{km}$ and $3\,\mathrm{km}$ for the outer and inner domain, respectively, with corresponding domain sizes of 500 × 400 and 300 × 300 grid points. The domain configuration is illustrated in Fig. 1. The vertical grid in both domains consists of 119 levels, extending to a model top at $10\,\mathrm{Pa}$ (approximately $63\,\mathrm{km}$). To reduce artificial wave reflection at the upper boundary, the model includes a damping layer in the upper $5\,\mathrm{km}$ of the vertical grid, following the approach of Kruse et al. (2022). Data within this damping layer are excluded from subsequent analysis, resulting in an effective model top near $58\,\mathrm{km}$.

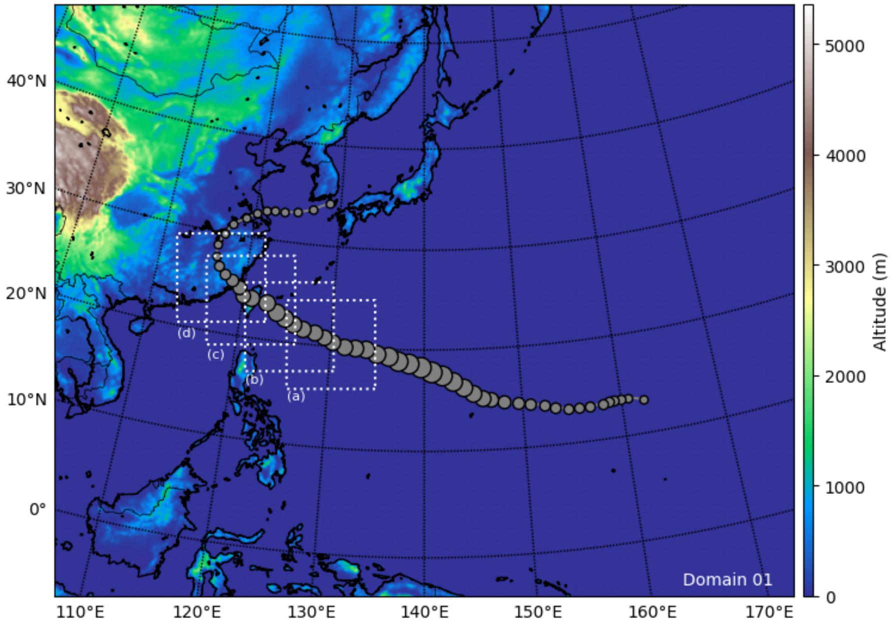

Figure 1. WRF model domain configuration showing the fixed outer domain (Domain 01) and the nested inner domain (Domain 02) overlaid on topography. Domain 01 provides the large-scale boundary forcing, while Domain 02 is implemented as a moving nest that follows the tropical cyclone center based on the IBTrACS best-track data. Grey circles indicate the IBTrACS storm track plotted at 6-hour intervals, with circle size proportional to the normalized tropical cyclone intensity relative to the first simulation hour. Boxes (a)–(d) show the locations of Domain 02 at +0, +24, +48, and +72 hours of simulation time, respectively.

The WRF model represents five primary physical processes: microphysics (MP), cumulus parameterization (CU), planetary boundary layer (PBL), radiation, and surface processes. These physics modules and parameterizations interact through model state variables and surface fluxes. The microphysics scheme represents water vapor, cloud, and precipitation processes, updating the corresponding state variables at each time step. More advanced microphysics schemes additionally represent ice-phase and mixed-phase processes, allowing for the formation of graupel or hail; such schemes are recommended for simulations with horizontal resolutions of $10\,\mathrm{km}$ or finer. The cumulus parameterization represents subgrid-scale convective and shallow cloud processes by parameterizing vertical fluxes associated with unresolved updrafts and downdrafts, and it also provides convective precipitation. Cumulus schemes are usually applied in simulations with grid spacings coarser than $10\,\mathrm{km}$. Accordingly, in this study, the cumulus parameterization is applied only in the Domain 01, while it is disabled in the nested Domain 02.

The PBL schemes account for vertical turbulent mixing and determine subgrid-scale flux profiles throughout the atmospheric column. Surface processes include surface layer schemes and land surface models. Surface layer schemes compute friction velocities using similarity theory and determine exchange coefficients for surface heat, moisture, and momentum fluxes, and are compatible only with specific PBL options. Land surface models calculate the exchange of energy and moisture between the lowest atmospheric layer and the land surface, accounting for interactions with vegetation, the subsurface (e.g., simplified

https://doi.org/10.5194/egusphere-2026-1469
Preprint. Discussion started: 23 April 2026

groundwater processes), and, where applicable, urban areas. Radiation schemes compute atmospheric heating rates and radiative fluxes by representing absorption, reflection, and scattering processes. Further details are provided in the WRF technical documentation by Skamarock et al. (2019).

The following physics parameterizations are selected to conduct a sensitivity analysis using different model configurations for the WRF simulation of TC Soudelor. Two microphysics schemes (WSM6 and Goddard) are considered, together with five planetary boundary layer (PBL) schemes (YSU, MYJ, GFS, ACM2, and BouLac). These schemes represent commonly used single-moment (WSM6) and more complex mixed-phase (Goddard) formulations in tropical cyclone modeling and span a representative range of microphysical complexity. In addition, simulations are performed with and without the Grell–3 cumulus parameterization. The selection of these two microphysics schemes, five PBL schemes, and the optional cumulus parameterization follows the study of Lu et al. (2023). Both the WSM6 and Goddard microphysics schemes are compatible with the Grell–3 cumulus scheme. To examine the impact of cumulus parameterization, the Grell–3 scheme is applied only in Physics Set 3 and is implemented exclusively in Domain 01. The complete set of fifteen physics combinations is listed in Table 1.

2.4 Model diagnostics

To evaluate the sensitivity of the simulated tropical cyclone and the associated stratospheric gravity waves to different physics configurations, a set of diagnostics is applied to the WRF simulations. These diagnostics are grouped into three categories: (i) tropical cyclone metrics, (ii) convection and latent heating proxies, and (iii) gravity wave characteristics. Post-processing of WRF output to obtain those diagnostics was performed using the `wrf-python` software package (Sizemore et al., 2022) as well as standard scientific Python packages.

2.4.1 Tropical cyclone metrics

The simulated tropical cyclone track and intensity are evaluated against IBTrACS observations. The storm center in the model output is identified as the grid point with the minimum sea-level pressure. Track error is computed as the horizontal distance between the simulated and observed storm centers at corresponding times. Storm intensity is characterized by both minimum sea-level pressure (MSLP) and maximum sustained wind speed (MSW). These standard metrics are used to assess whether different physics configurations produce comparable large-scale TC evolution within observational uncertainty, providing a baseline for interpreting differences in convection and gravity wave characteristics.

2.4.2 Convection and latent heating diagnostics

Convective activity in the simulations is characterized using relevant proxies for deep convection and latent heat release. Outgoing longwave radiation (OLR) is used as an indicator of cloud top height and convective intensity, enabling direct comparison with satellite observations. In addition, the latent heating rate (LHR) is used as a physically based proxy for diabatic heating associated with moist convection. The LHR is calculated from the temporal tendencies of hydrometeor mixing ratios produced

https://doi.org/10.5194/egusphere-2026-1469
Preprint. Discussion started: 23 April 2026

Table 1. Physics configurations used in the WRF sensitivity experiments, grouped into three sets. Each case combines a microphysics scheme, a planetary boundary layer (PBL) scheme, and an optional cumulus parameterization.

Index	Microphysics	PBL	Cumulus
Physics Set 1			
1	WSM6	YSU	-
2	WSM6	MYJ	-
3	WSM6	GFS	-
4	WSM6	ACM2	-
5	WSM6	BouLac	-
Physics Set 2			
6	Goddard	YSU	-
7	Goddard	MYJ	-
8	Goddard	GFS	-
9	Goddard	ACM2	-
10	Goddard	BouLac	-
Physics Set 3			
11	WSM6	YSU	Grell-3
12	WSM6	MYJ	Grell-3
13	WSM6	GFS	Grell-3
14	WSM6	ACM2	Grell-3
15	WSM6	BouLac	Grell-3

by the microphysics schemes, combined with the corresponding latent heats of phase changes. It is defined as

$$\mathrm{LHR} = \frac{1}{C_p}\left(L_v\frac{\Delta q_c + \Delta q_r}{\Delta t} + L_f\frac{\Delta q_i}{\Delta t} + L_s\frac{\Delta q_s + \Delta q_g}{\Delta t}\right), \quad (1)$$

where q_c, q_r, q_i, q_s, and q_g denote the mixing ratios of cloud water, rain water, ice, snow, and graupel, respectively. The latent heats of vaporization, fusion, and sublimation are $L_v = 2.5\times10^6\,\mathrm{J\,kg^{-1}}$, $L_f = 3.34\times10^5\,\mathrm{J\,kg^{-1}}$, and $L_s = 2.834\times10^6\,\mathrm{J\,kg^{-1}}$, and $C_p = 1{,}004.0\,\mathrm{J\,kg^{-1}\,K^{-1}}$ is the specific heat capacity at constant pressure. The time interval $\Delta t = 900\,\mathrm{s}$ corresponds to the 15-minute model output frequency. The spatial distribution and vertical structure of LHR are analyzed to diagnose differences in convective structure and diabatic forcing among the different physics configurations.

2.4.3 Gravity wave diagnostics

Gravity wave characteristics are diagnosed from the simulated vertical velocity field in the stratosphere and lower mesosphere. In this altitude range, vertical motions are largely dominated by gravity waves rather than by balanced or convective flows, making vertical velocity a particularly sensitive and direct indicator of gravity wave activity. Our analysis therefore focuses on gravity wave amplitudes and spectral characteristics derived from the vertical velocity field, enabling consistent comparison across different model physics configurations.

To characterize the spatially varying spectral properties of the simulated gravity wave fields, we perform a localized spectral analysis using the S-transform. The S-transform is a time–frequency (or space–wavenumber) analysis technique that combines elements of the short-time Fourier transform and wavelet analysis, providing localized information on gravity wave amplitude, phase, and dominant horizontal and vertical wavenumbers. The method is particularly well suited for analyzing gravity waves generated by localized and transient sources such as tropical cyclones, where wave properties can vary substantially in space and time. S-transform methods have been successfully applied to both satellite observations and model simulations of gravity waves in the stratosphere (Hindley et al., 2016; Wright et al., 2017; Hindley et al., 2019). In this study, the S-transform is applied to the simulated gravity waves in the vertical velocity fields to quantify differences in wave amplitude and spectral characteristics among the different physics configurations. The S-transform analysis is applied only to Domain 02, which resolves convection explicitly at 3 km grid spacing.

To facilitate statistical comparison across the fifteen simulations, kernel density estimation (KDE) is applied to selected gravity wave diagnostics derived from the S-transform analysis. The KDE provides a smooth estimate of the probability density function of a variable x and is defined as:

$$f_h(x) = \frac{1}{nh}\sum_{i=1}^{n} K\left(\frac{x_i - x}{h}\right), \tag{2}$$

where n is the sample size, h is the bandwidth, and K is the kernel function. A Gaussian kernel is used for smoothing:

$$K(u) = \frac{1}{\sqrt{2\pi}} \exp\left(-\frac{1}{2}u^2\right). \tag{3}$$

The bandwidth h was selected empirically to provide a suitable balance between smoothing and preserving meaningful structure in the distributions, reducing spurious oscillations while retaining the main features of the gravity wave parameter distributions. Normalized cumulative KDEs (Lu et al., 2023) are employed to compare the distributions of gravity wave properties across the different physics configurations in a consistent manner.

3 Results

3.1 Observed gravity waves and cloud structure during Typhoon Soudelor

To provide observational context and motivate the subsequent modeling analysis, AIRS/Aqua satellite observations are used to illustrate the presence of stratospheric gravity waves associated with Typhoon Soudelor. AIRS was selected because it has proven effective in detecting and characterizing TC-induced gravity waves in previous studies, owing to its relatively high horizontal resolution and sensitivity to small temperature perturbations in the middle and upper stratosphere. During Soudelor's

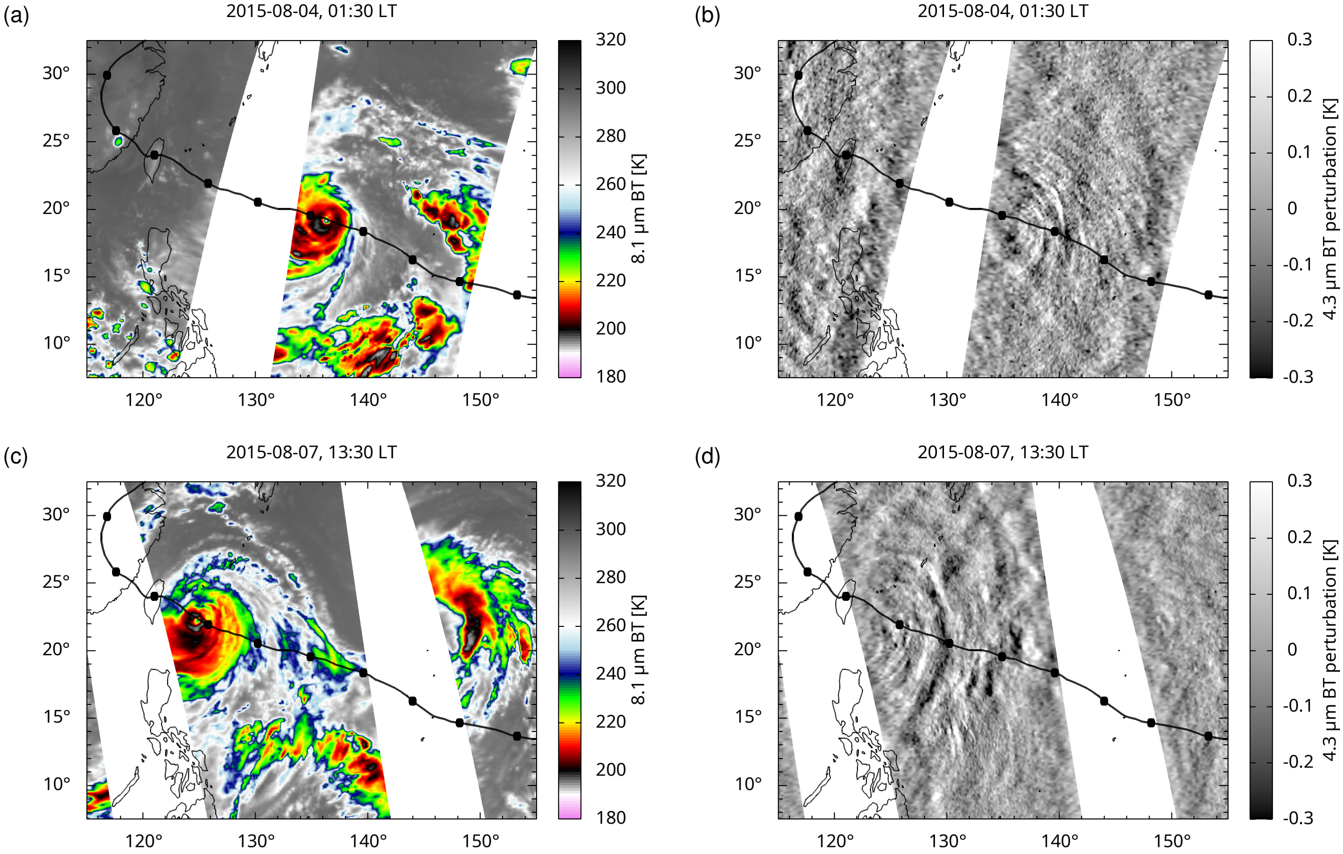

Figure 2. AIRS/Aqua observations of Typhoon Soudelor on 4 August 2015, approximately 01:30 LT, and 7 August 2015, approximately 13:30 LT. Panels (a, c) show cloud top brightness temperatures at 8.1 μm, while panels (b, d) show brightness temperature perturbations at 4.3 μm, highlighting semi-circular stratospheric gravity waves located upstream of the convective sources under easterly background winds. The black curve denotes the storm track from IBTrACS, and black circles indicate 3-hourly time intervals.

lifetime, the AIRS observations reveal pronounced and coherent stratospheric gravity wave activity, making this storm a well-suited case for further investigation. The presence of strong, well-organized wave patterns provides clear motivation for targeted WRF simulations aimed at examining how gravity wave generation and structure relate to the storm's convective features under different physics configurations.

Figure 2 presents AIRS observations of stratospheric gravity waves and associated cloud structures during two satellite overpasses of TC Soudelor on 4 August 2015 at approximately 01:30 LT (nighttime) and 7 August 2015 at approximately 13:30 LT (daytime). Panels (b) and (d) show brightness temperature perturbations in the 4.3 μm CO_2 band, in which gravity waves appear as alternating warm and cold bands forming distinct semi-circular patterns radiating outward from the storm. These wave signatures are predominantly located upstream of the main convective regions, consistent with easterly background winds that favor upstream wave propagation with relatively long vertical and short horizontal wavelengths. These are wave characteristics to which AIRS, as a nadir-viewing instrument, is particularly sensitive. Panels (a) and (c) display coincident cloud top brightness temperatures at $8.1\,\mu\mathrm{m}$, illustrating the spatial extent and organization of deep convective clouds within the typhoon. Together, these observations allow a direct comparison between the stratospheric gravity wave field and the underlying convective structure, illustrating the close coupling between tropical cyclone convection and gravity wave generation.

While the WRF simulations are designed to realistically capture the large-scale evolution of Typhoon Soudelor and its convective structure, reproducing the exact spatial phase and fine-scale patterns of individual gravity wave packets observed by AIRS is not expected in general. Gravity wave generation by tropical cyclones is inherently sensitive to the detailed temporal and spatial variability of convective sources, as well as to the evolving background wind and stability profiles. As a result, the modeling analysis focuses on robust statistical and structural characteristics of the gravity wave field, such as amplitude, vertical propagation, and spectral properties, rather than one-to-one replication of individual observed wave patterns.

3.2 Simulated tropical cyclone track and intensity

We first evaluate the simulated tropical cyclone track and intensity to assess the realism of the WRF simulations of Typhoon Soudelor before examining the associated gravity wave response. The simulations are compared with IBTrACS best-track data. Figure 3a shows the simulated TC tracks for all physics configurations, performed without (Physics Sets 1 and 2) and with (Physics Set 3) cumulus parameterization. During the early and mature oceanic phase of the storm, all simulated tracks closely follow the IBTrACS best track. Across all physics configurations, the simulated track errors remain within $100\,\mathrm{km}$ for approximately the first 45 h of the simulation (Fig. 3b), indicating good agreement with the best-track data during this period.

After approximately 45 h, larger deviations from the IBTrACS best track develop in all simulations. This timing coincides with the approach of Typhoon Soudelor toward Taiwan and the onset of land interaction. While the observed storm makes landfall in central Taiwan, all simulated storms exhibit a systematic displacement and instead drift toward northern Taiwan. This behavior is consistent across physics configurations and indicates a common model bias during the landfall phase rather than sensitivity to individual physics parameterizations, likely reflecting the influence of the large-scale environmental flow imposed by the initial and lateral boundary conditions. Given this limitation, we primarily focus our analysis on the first 45 h of the simulations, although relative differences between physics configurations beyond this time may still retain physical meaning despite increasing deviations from the best-track data.

Despite the similarity of the simulated tracks, subtle systematic differences among physics configurations are apparent. Simulations that include the cumulus parameterization (Physics Set 3) reveal a wider spread of track positions across different PBL schemes, but slightly smaller mean track errors compared to simulations without cumulus parameterization (Physics Sets 1 and 2), with the exception of configurations using the ACM2 PBL scheme. As shown in Table 2, simulations using the Goddard microphysics scheme yield the largest average track error among the configurations. Relative to Goddard, WSM6 and WSM6–Grell-3 reduce the average error by 6.4% and 22.3%, respectively. Overall, the WSM6–YSU–Grell-3 configuration produces the smallest mean track error within the first 45 h of the simulation, while Goddard–BouLac produces the largest error.

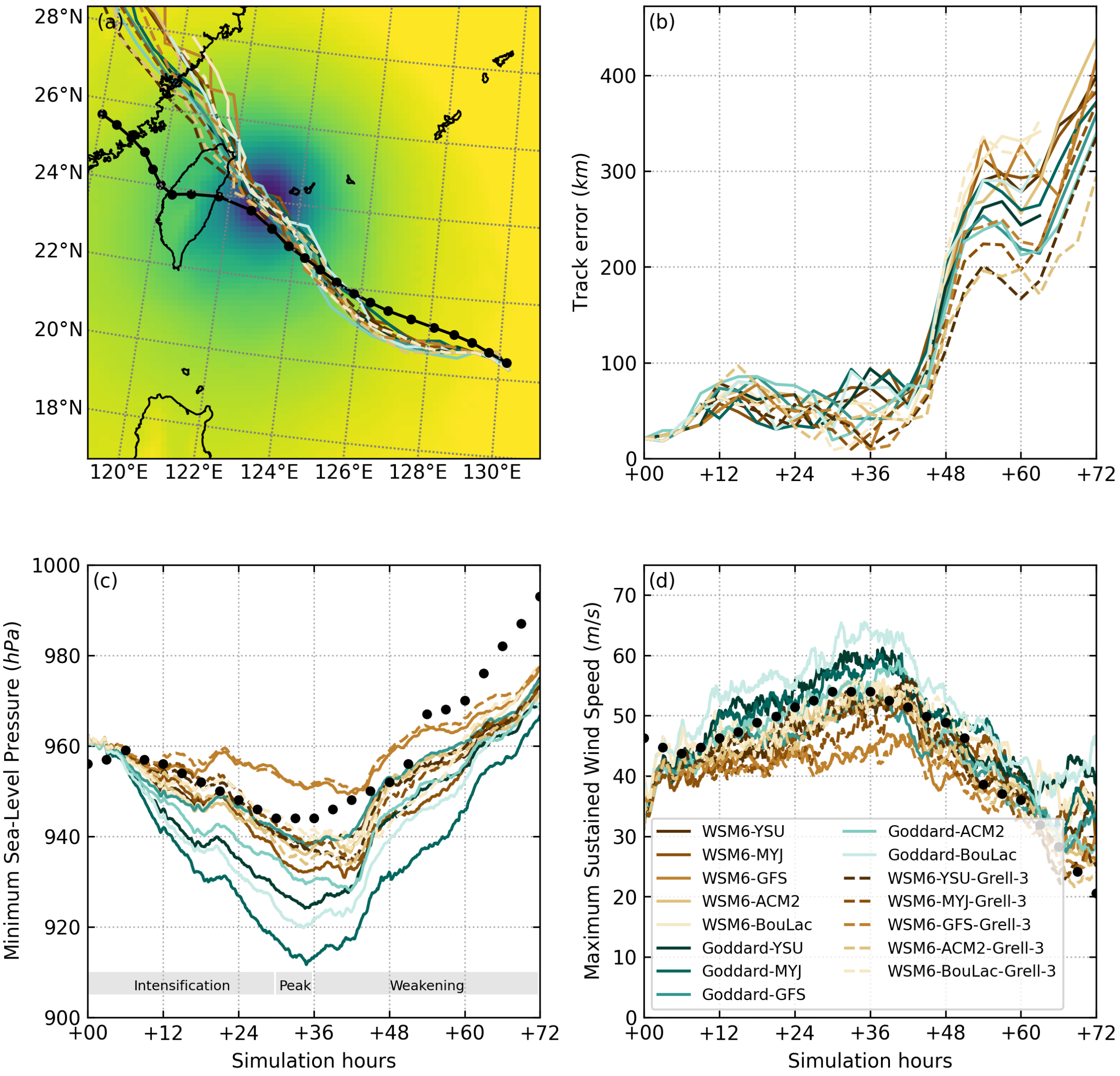

Figure 3. Simulated tropical cyclone tracks for Typhoon Soudelor compared with the IBTrACS best-track data: (a) simulated and IBTrACS best-track TC positions, (b) distance between the simulated and best-track TC centers, (c) minimum sea-level pressure (MSLP), and (d) maximum sustained wind speed (MSW). The legend in (d) identifies the different WRF simulations and physics configurations.

The simulated TC tracks in this study are broadly consistent with previous modeling studies of Typhoon Soudelor. For example, Li and Huang (2019) reported a systematic northward bias in simulated tracks using the Hurricane Weather Research and Forecasting (HWRF) model with NCEP GDAS as initial and boundary conditions, in which storms were displaced toward northern Taiwan rather than central Taiwan, consistent with the northward displacement found in our simulations. However,

https://doi.org/10.5194/egusphere-2026-1469
Preprint. Discussion started: 23 April 2026

Chane Ming et al. (2019) found a slightly southward landfall bias using WRF-ARW, although their study provides less detail on the subsequent track evolution.

Figures 3c,d compare the simulated TC intensity with IBTrACS best-track data in terms of minimum sea-level pressure (MSLP) and maximum sustained wind speed (MSW). Simulations using the Goddard microphysics scheme generally produce stronger storms than those using WSM6, while the WSM6–GFS configuration yields the weakest simulated intensity. Except for the WSM6–GFS case, most simulations overestimate TC intensity relative to the best-track data. Simulations using Goddard microphysics also tend to weaken the storm earlier than those using WSM6. However, most physics configurations fail to reproduce the rapid weakening observed after 54 h. This deviation coincides with the period when the simulated TC tracks begin to diverge from the best-track estimate, following the onset of land interaction and the northward displacement of the simulated storms. The delayed weakening in the simulations is therefore expected, as the simulated storms do not experience land interaction comparable to that in the observed case.

3.3 Cloud and convective structure from simulated and observed OLR

To further evaluate the simulated storm structure during the pre-landfall period, simulated outgoing longwave radiation (OLR) from the WRF model is compared with satellite-derived OLR from the FengYun-2G satellite. This comparison allows us to assess how different physics configurations represent cloud structure and convective activity, which are closely linked to latent heat release. Figures 4–6 show simulated OLR fields at 03:00 UTC on 7 August 2015 (+27 h of simulation time) for Physics Sets 1–3, respectively, alongside the corresponding FengYun-2G observations.

Simulations using WSM6 microphysics with the Grell–3 cumulus parameterization (Physics Set 3; Fig. 6) produce more extensive low-level cloud cover than the other physics configurations and than indicated by the satellite observations. These simulations also fail to capture the additional tropical disturbance located between 140°E and 150°E, which is clearly visible in the satellite observations. In contrast, simulations using the Goddard microphysics scheme (Physics Set 2; Fig. 5) generate less widespread cloud cover than the WSM6–Grell–3 configuration but exhibit stronger convective signatures associated with both Typhoon Soudelor and the nearby tropical disturbance than the WSM6 configurations without cumulus parameterization (Physics Set 1; Fig. 4). Compared with Physics Sets 1 and 3, the Goddard microphysics simulations more clearly reproduce localized regions of deep convection, consistent with the lower OLR values found in the satellite observations and indicative of stronger localized convective heating that can act as a source of gravity waves.

Table 2. Mean track errors (km) of Typhoon Soudelor during the first 45 h of the simulations for different microphysics and planetary boundary layer (PBL) scheme combinations. The set mean denotes the average across the five PBL schemes.

Microphysics	YSU	MYJ	GFS	ACM2	BouLac	Set mean
WSM6	50.5	51.7	43.9	52.0	51.3	49.9
Goddard	53.9	50.0	53.5	56.1	52.8	53.3
WSM6-Grell-3	38.0	41.8	39.7	47.2	40.5	41.4

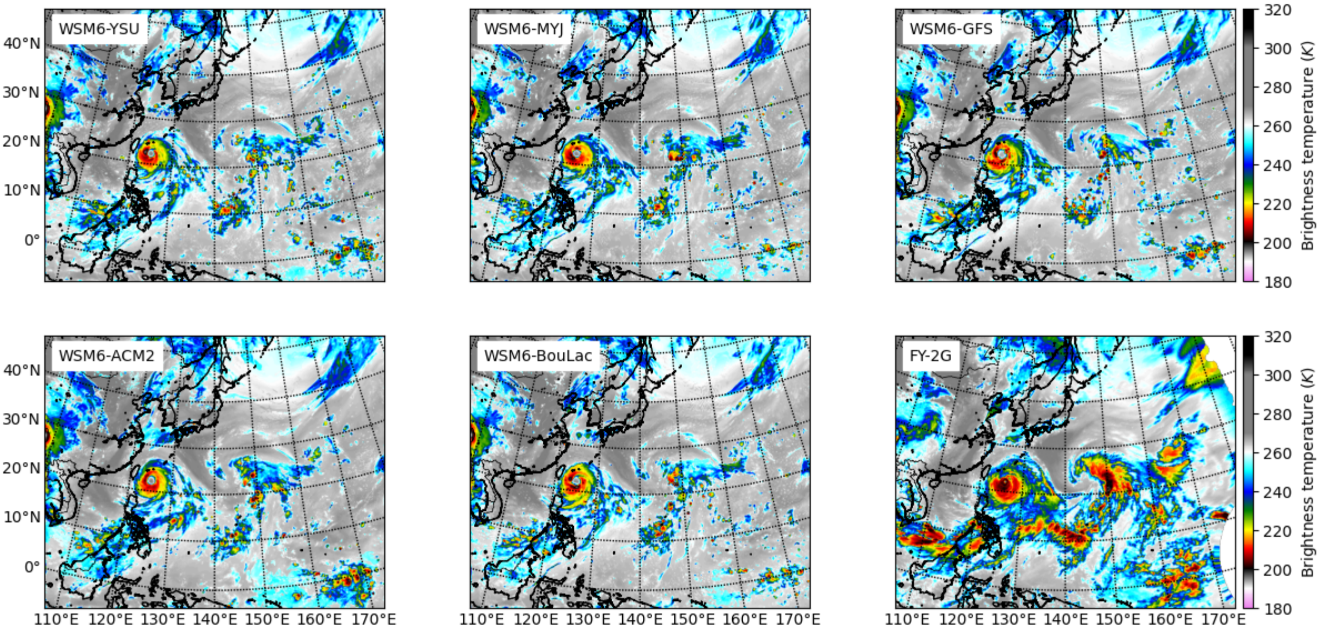

Figure 4. Simulated outgoing longwave radiation (OLR), shown as brightness temperature, at +27 h of simulation time (03:00 UTC on 7 August 2015) for Physics Set 1 (WSM6 microphysics), compared with FengYun-2G satellite observations.

To further quantify differences in cloud-top characteristics among the physics configurations, kernel density estimates (KDEs) of OLR brightness temperatures are computed for Domain 01 over the range 190–260 K (Fig. 7). At brightness temperatures below 220 K, corresponding to the coldest cloud tops and most relevant for diagnosing intense deep convection, the simulated OLR distributions separate into three distinct groups reflecting differences in microphysics and the use of cumulus parameterization. Such cold cloud tops are typically associated with strong localized diabatic heating and therefore indicate potential sources of gravity wave generation. Simulations using the Goddard microphysics scheme (Physics Set 2) exhibit the strongest and most frequent deep convective signatures and show the best agreement with satellite observations, followed by WSM6 simulations without cumulus parameterization (Physics Set 1). In contrast, simulations using the Grell–3 cumulus scheme (Physics Set 3) tend to produce more widespread cloud cover but underestimate the occurrence of the coldest cloud tops associated with intense deep convection. At brightness temperatures above 250 K, simulations with all physics configurations overestimate cloud occurrence relative to the satellite observations, indicating an excessive representation of warmer, low-level clouds in the simulations. In addition, simulations using the Goddard microphysics scheme show a slight underestimation of cloud occurrence in the intermediate OLR range between approximately 225 and 245 K.

The differences in simulated OLR and cloud-top brightness temperature distributions indicate systematic variations in convective organization and cloud depth among the physics configurations. Because latent heat release associated with moist convection is the primary forcing mechanism for tropical cyclone–generated gravity waves, these differences are expected to

https://doi.org/10.5194/egusphere-2026-1469
Preprint. Discussion started: 23 April 2026

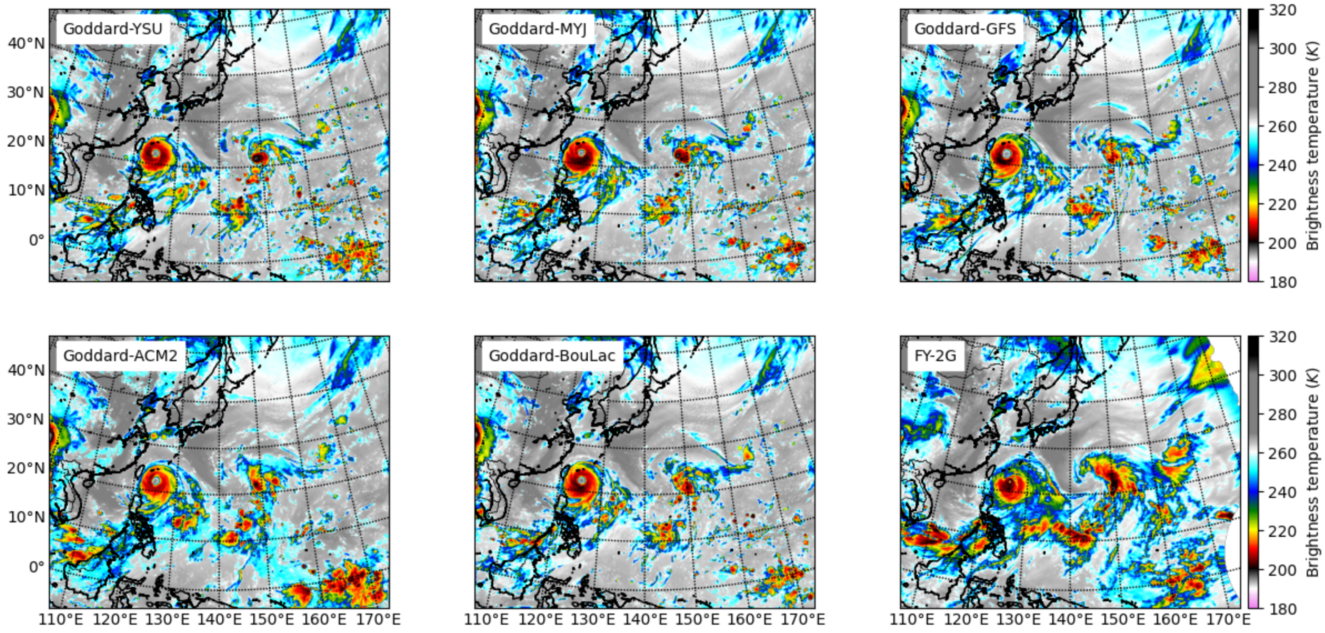

Figure 5. Same as Fig. 4 but for Physics Set 2 (Goddard microphysics).

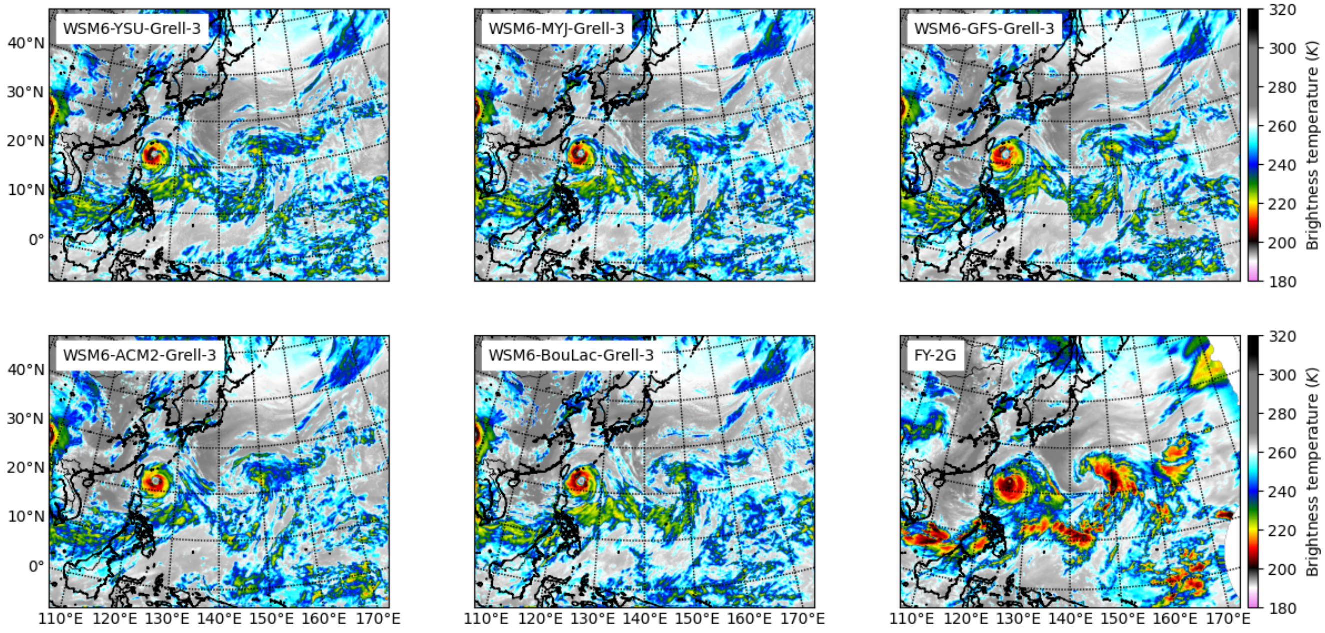

Figure 6. Same as Fig. 4 but for Physics Set 3 (WSM6 microphysics with Grell-3 cumulus parameterization).

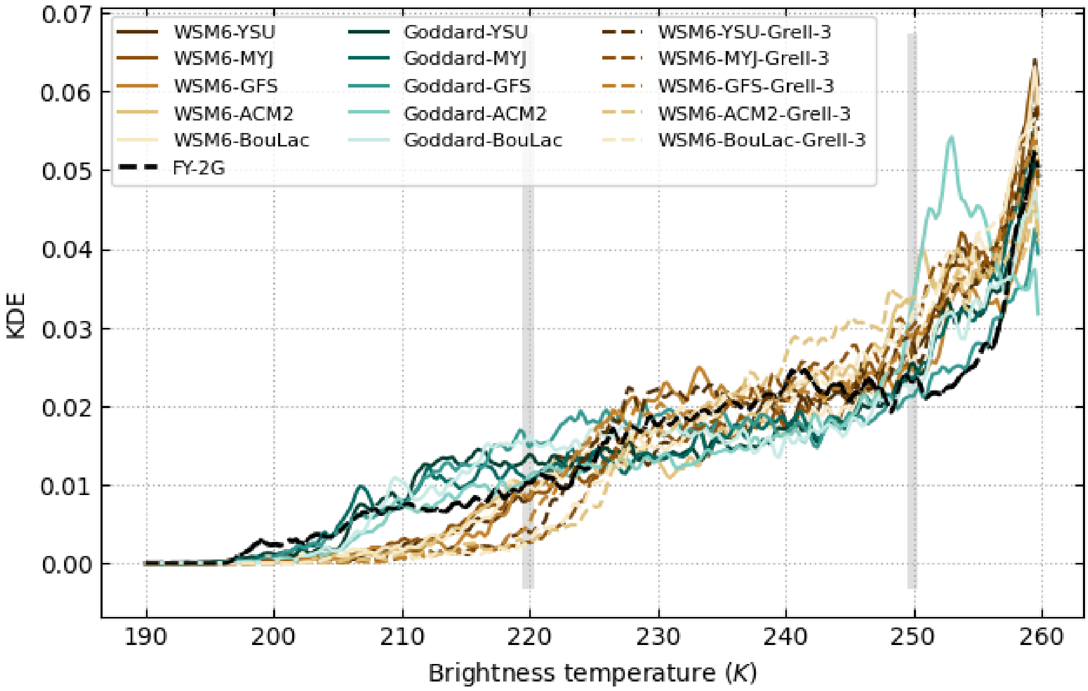

Figure 7. Kernel density estimates (KDEs) of OLR brightness temperatures across Domain 01 at +27 h of simulation time for all physics configurations (15 cases), shown over the range 190–260 K. The two grey zones shows the temperature between 220 and 225 and the one between 250 and 255.

translate into distinct spatial and vertical structures of latent heating. We therefore next examine the simulated latent heating rates to directly assess how model physics choices modify the vertical and spatial characteristics of diabatic heating.

3.4 Sensitivity of latent heating structure to model physics

Large latent heat release in tropical cyclones is primarily associated with deep moist convection. As air rises within convective updrafts, it cools and water vapor condenses, releasing substantial amounts of latent heat through phase changes. This diabatic heating typically occurs throughout the mid to upper troposphere, where it helps sustain convective updrafts and organize the storm's convective structure. The thermal forcing associated with latent heat release is also one of the primary mechanisms for gravity wave generation. In particular, the vertical structure and intensity of the heating strongly influence the dominant vertical wavelength, horizontal phase speed, and the resulting gravity wave momentum flux spectrum (Alexander et al., 1995; Lane et al., 2001; Beres et al., 2002; Richter et al., 2010; Alexander et al., 2021). It is therefore informative to compare both the magnitude and vertical distribution of latent heat release across different physics parameterization schemes. Differences in latent heating among the schemes can help explain variations in the gravity wave amplitudes and spectral characteristics simulated under different model configurations.

https://doi.org/10.5194/egusphere-2026-1469
Preprint. Discussion started: 23 April 2026

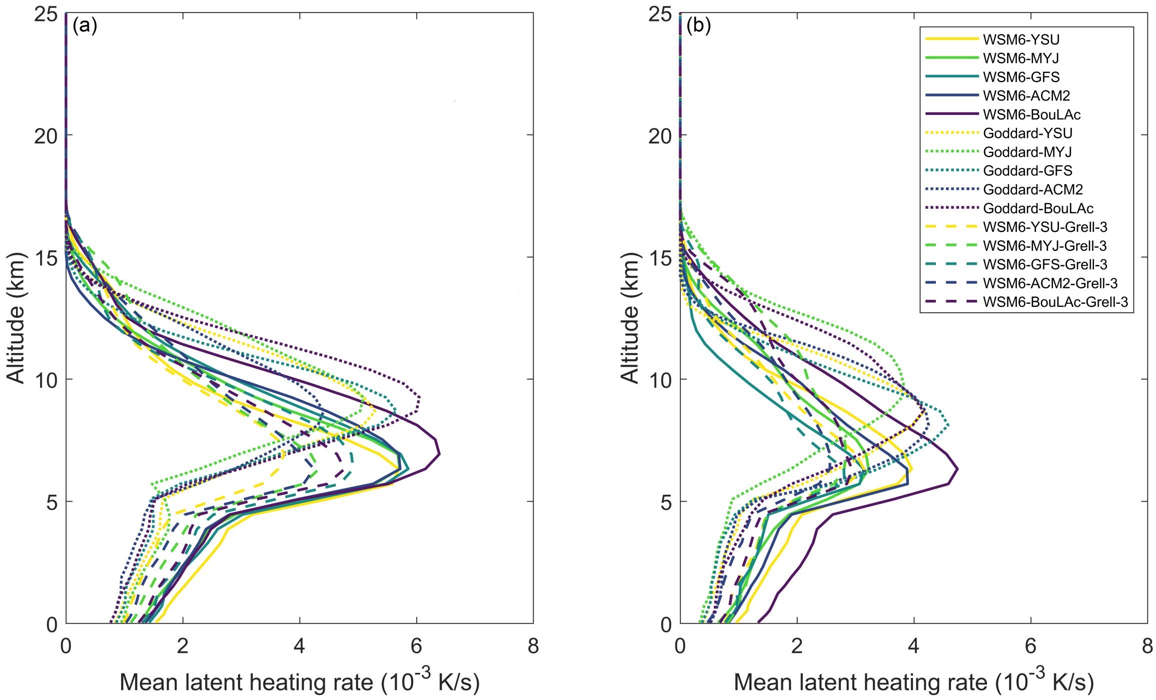

Figure 8. Mean vertical profiles of strong latent heating rates (LHR) at (a) +27 h and (b) +36 h of simulation time, computed from grid points exceeding the 95th percentile of the vertically averaged LHR. The profiles demonstrate differences in heating magnitude and peak altitude among the physics configurations.

In this study, the latent heating rate (LHR) is used as a proxy for latent heat release. The LHR is calculated from the temporal tendencies of hydrometeor mixing ratios produced by the microphysics scheme, combined with the corresponding latent heats of phase changes for cloud water, rain, ice, snow, and graupel. The analysis focuses on regions of strong latent heating associated with deep convection. Specifically, we first compute the vertically averaged LHR within the mid- to upper troposphere (from $5\,\mathrm{km}$ to $15\,\mathrm{km}$ altitude). We then identify grid points where the vertically averaged LHR exceeds the 95th percentile of the domain-wide LHR distribution. The mean vertical profile of strong latent heating is obtained by horizontally averaging positive LHR values at these grid points. This approach isolates the most intense and dynamically relevant heating regions, which are expected to play a key role in gravity wave generation. The results are qualitatively similar when using a 90th percentile threshold.

The mean vertical profiles of strong latent heating rates (LHR) at two selected stages of the simulation are shown in Fig. 8. To facilitate comparison, we focus on two representative time steps: +27 h, corresponding to the intensification phase of Typhoon Soudelor, and +36 h, representing the period of peak storm intensity. The latent heating rates are generally larger during the intensification phase of the tropical cyclone, reaching localized values of up to $6 \times 10^{-3}\,\mathrm{K\,s^{-1}}$, and smaller during the period of peak storm intensity (around $4\times10^{-3}\,\mathrm{K\,s^{-1}}$ to $5\times10^{-3}\,\mathrm{K\,s^{-1}}$). This behavior is consistent with more intermittent and localized convective activity and stronger localized diabatic forcing during intensification, whereas heating becomes more spatially distributed and temporally smoother at peak intensity. Parameterization schemes employing the Goddard microphysics scheme tend to produce maximum LHR values at higher altitudes (around $10\,\mathrm{km}$) compared with WSM6 (around $7\,\mathrm{km}$), suggesting that gravity wave source regions may be located at greater heights in simulations using the Goddard scheme. Because the vertical location of diabatic heating strongly influences the vertical wavelength and propagation characteristics of gravity waves, these differences in heating altitude may contribute to differences in the simulated gravity wave spectra. In contrast, schemes that include the cumulus parameterization (Grell–3) yield smaller LHR magnitudes and lower peak heating values during the selected periods.

Figure 9 compares the mean vertical depth of the peak LHR profiles for the different parameterization schemes. The LHR depth is determined for each vertical profile identified by the 95th-percentile criterion described above. For each profile, the altitude of the maximum LHR is first identified. Starting from this peak level, the profile depth is then determined by searching upward and downward independently until the first level at which LHR falls below $20\,\%$ of the peak value is encountered in each direction. The vertical distance between these two bounding levels defines the heating-layer depth. The mean LHR depth is subsequently obtained by averaging these depths across all selected profiles, thereby isolating the vertically coherent and dynamically significant heating layers associated with deep convection. Latent heating is generally deeper under WSM6 microphysics (exceeding $10\,\mathrm{km}$) than under Goddard microphysics (typically below $10\,\mathrm{km}$). This distinction persists at both +27 h and +36 h and suggests that gravity waves generated in simulations using the Goddard scheme may preferentially exhibit shorter vertical wavelengths. Although the inclusion of the cumulus parameterization reduces the magnitude of LHR, it produces similar vertical heating depths compared with simulations using the same microphysics and planetary boundary layer schemes.

The differences in the magnitude and vertical extent of latent heating across the physics configurations imply substantial variations in the forcing of gravity waves by Typhoon Soudelor. Because gravity wave amplitude and vertical wavelength are strongly controlled by the depth and intensity of diabatic heating, these differences are expected to produce distinct gravity wave responses in the stratosphere. We now examine how the simulated stratospheric gravity wave fields vary among the different physics configurations in terms of their amplitude and spectral characteristics.

3.5 Stratospheric gravity wave variability diagnosed from vertical velocity

Gravity wave activity in the simulations is diagnosed using the variability of vertical velocity, quantified by the standard deviation of the vertical wind component (w). In the stratosphere, gravity waves are a primary contributor to vertical velocity variability, and the standard deviation of w therefore provides a useful proxy for gravity wave amplitude that is independent of wave phase. This metric is used throughout this subsection to compare gravity wave activity across the different physics configurations.

Figure 10 shows the domain-averaged standard deviation of vertical velocity at two stratospheric levels, approximately $21\,\mathrm{km}$ (lower stratosphere) and $39\,\mathrm{km}$ (upper stratosphere), within Domain 02 for all simulations. A period of enhanced gravity wave

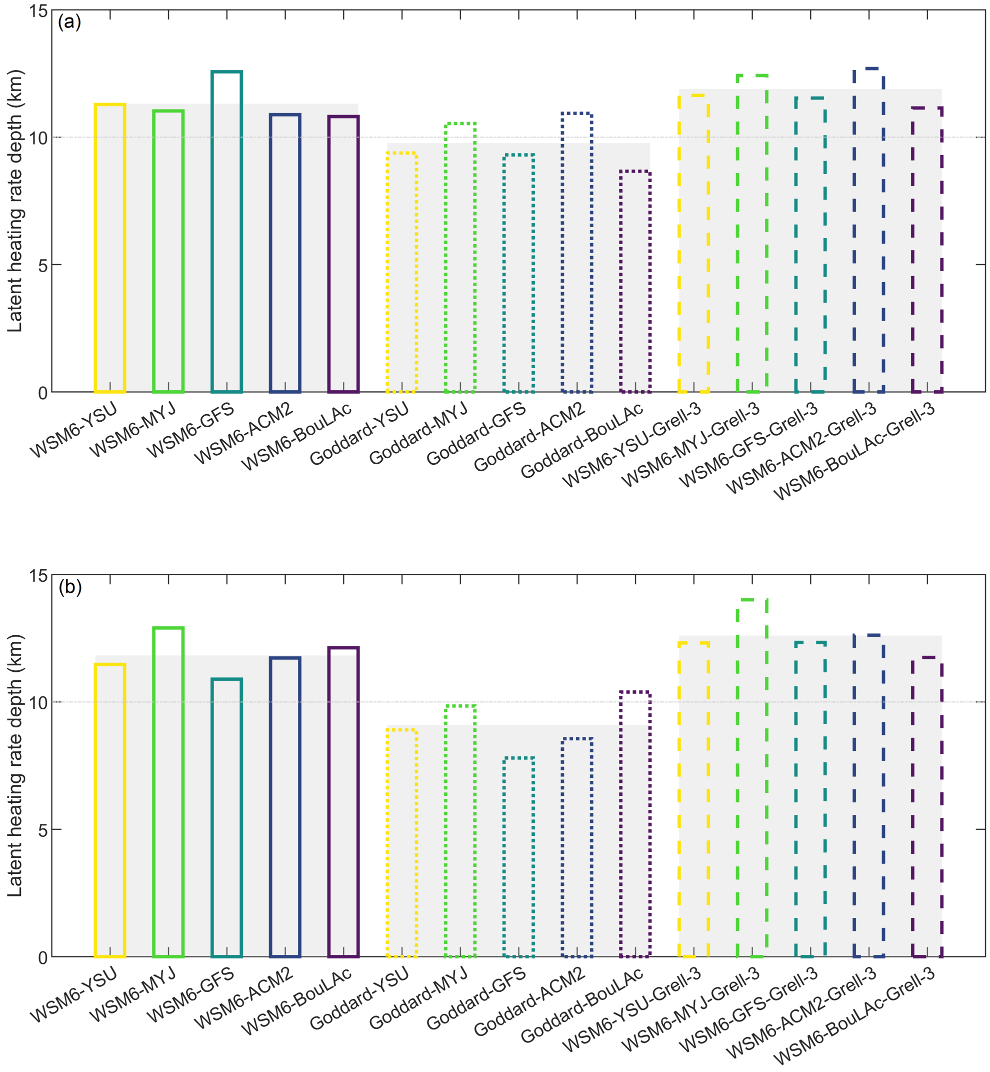

Figure 9. Mean vertical depth of strong latent heating rates (LHR) for the different physics configurations at (a) +27 h and (b) +36 h of simulation time. The heating depth is defined as the vertical extent around the LHR maximum where LHR remains above 20 % of its peak value for profiles exceeding the 95th percentile criterion. Gray bars indicate the mean depth averaged across each group of five physics schemes.

activity is evident near +27 h, corresponding to the intensification phase of Typhoon Soudelor and consistent with the stronger and more localized latent heating discussed in the previous subsection, whereas +36 h represents the period of peak storm intensity. At 39 km, the standard deviation of vertical velocity across the simulations ranges from approximately $0.8\,\mathrm{m\,s^{-1}}$ to $1.9\,\mathrm{m\,s^{-1}}$ near +27 h and from about $0.6\,\mathrm{m\,s^{-1}}$ to $1.6\,\mathrm{m\,s^{-1}}$ near +36 h. At 21 km, the corresponding variability is smaller, ranging from roughly $0.18\,\mathrm{m\,s^{-1}}$ to $0.43\,\mathrm{m\,s^{-1}}$ at +27 h and from $0.18\,\mathrm{m\,s^{-1}}$ to $0.37\,\mathrm{m\,s^{-1}}$ at +36 h.

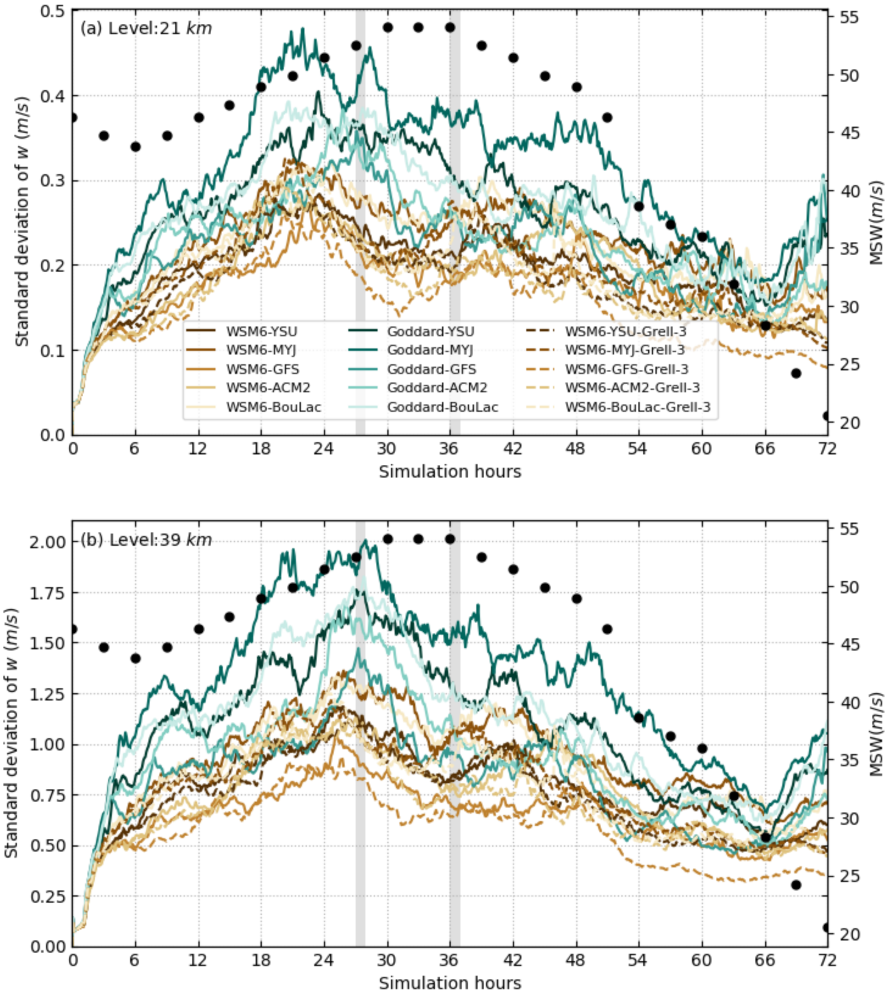

Figure 10. Time series of the domain-averaged standard deviation of vertical velocity w at (a) $21\,\mathrm{km}$ (lower stratosphere) and (b) $39\,\mathrm{km}$ (upper stratosphere) within Domain 02 for all physics configurations. The standard deviation of w serves as a proxy for stratospheric gravity wave activity. The gray bars at 27 h and 36 h denote the selected intensification phase and peak-intensity periods used for subsequent gravity wave analyses. Black dots indicate tropical cyclone intensity from IBTrACS, expressed as maximum sustained wind (MSW; right y-axis).

The larger range of vertical velocity values at $39\,\mathrm{km}$ reflects the amplification of gravity wave amplitudes with decreasing air density in the upper stratosphere. Although substantial temporal variability is present among the simulations, gravity wave activity is generally stronger during the TC intensification stage and relatively weaker at peak intensity. Differences between physics configurations are also apparent. Simulations grouped by planetary boundary layer (PBL) scheme indicate that the MYJ scheme produces larger vertical velocity variability, particularly during the first peak period when combined with the Goddard microphysics scheme. More broadly, simulations employing the Goddard microphysics scheme exhibit stronger ver-

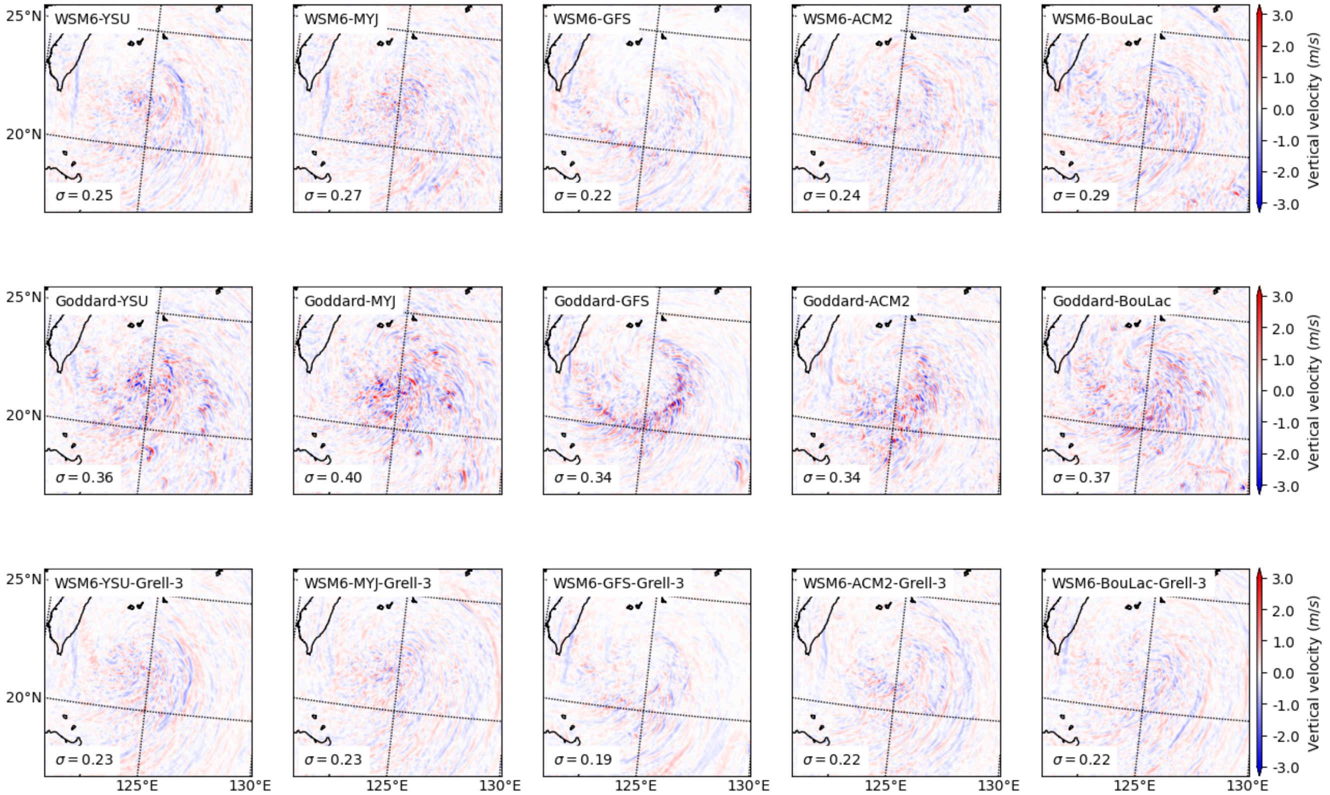

Figure 11. Spatial distribution of vertical velocity w at $21\,\mathrm{km}$ (lower stratosphere) in Domain 02 at +27 h for all physics configurations. Alternating regions of upward and downward motion indicate stratospheric gravity wave bands. The colorbar range is limited to $\pm 3\,\mathrm{m\,s^{-1}}$ to allow better comparison among the simulations. Each panel includes text labels indicating the domain-averaged standard deviation of w as well as the minimum and maximum values within the domain.

tical velocity variability than those using WSM6, indicating enhanced stratospheric gravity wave activity and larger gravity wave amplitudes.

Although IBTrACS observations indicate that Typhoon Soudelor reaches its peak intensity at approximately +30 to +36 h, the simulated gravity wave activity peaks earlier, during the period of rapid TC intensification. This timing is consistent with previous observational and modeling studies (Hoffmann et al., 2018; Wright, 2019; Wu et al., 2022, 2025), which show that TC intensification is statistically accompanied by increased stratospheric gravity wave activity, whereas TC weakening is associated with reduced wave activity. This relationship arises from stronger and deeper convective bursts during intensification, which enhance latent heat release and act as efficient sources of high-frequency gravity waves that propagate rapidly into the stratosphere. Consequently, stratospheric gravity wave activity may peak prior to the maximum surface intensity, reflecting the evolution of convective forcing rather than the storm's mature dynamical state.

https://doi.org/10.5194/egusphere-2026-1469
Preprint. Discussion started: 23 April 2026

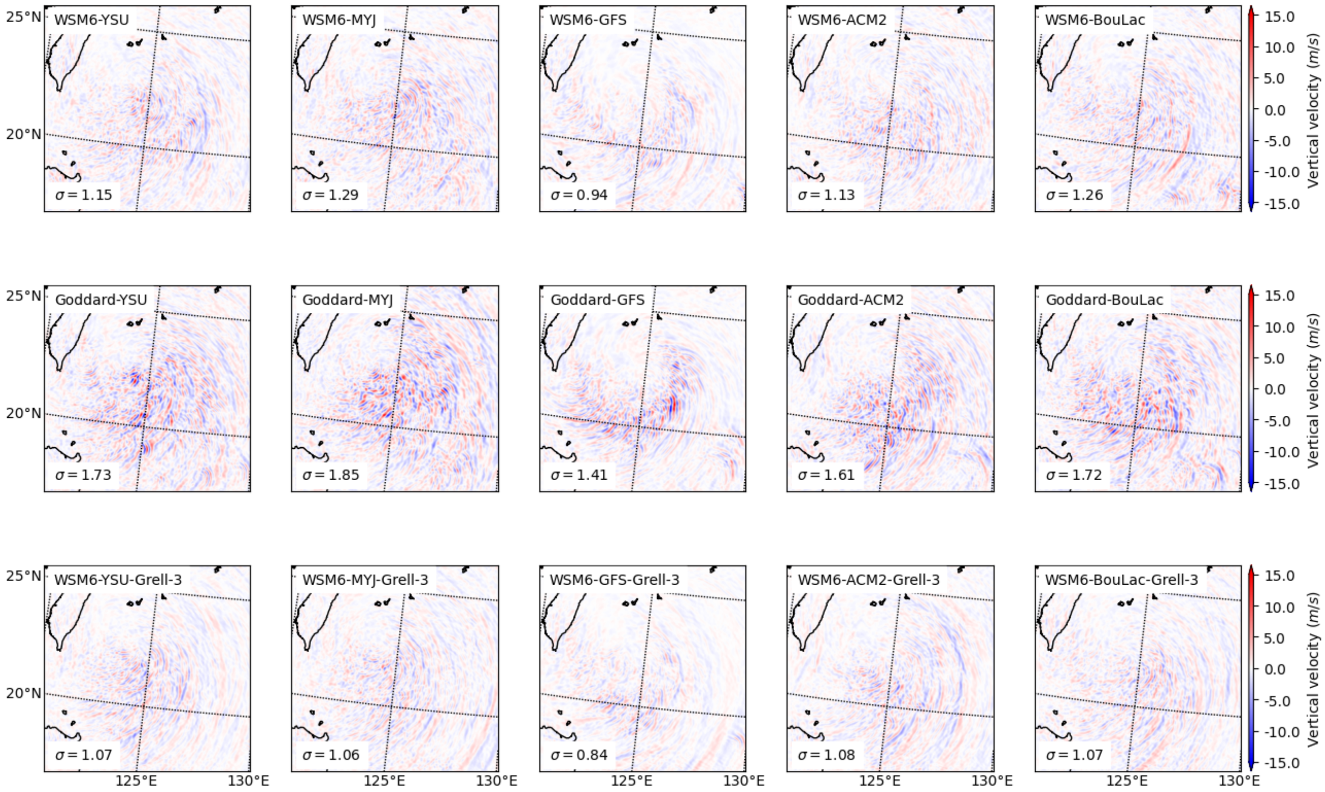

Figure 12. Same as Fig. 11, but for 39 km (upper stratosphere). The colorbar range is limited to $\pm 15\,\mathrm{m\,s^{-1}}$.

To further illustrate differences in the simulated gravity wave fields among physics configurations, Figs. 11 and 12 show the spatial distribution of vertical velocity at +27 h at two stratospheric levels, 21 km and 39 km, respectively. At 39 km, vertical velocity amplitudes are generally larger than at 21 km, consistent with the amplification of gravity wave amplitudes with decreasing air density in the upper stratosphere. Simulations using the Goddard microphysics scheme produce noticeably larger gravity wave amplitudes than those using WSM6, indicating stronger wave generation and a stronger stratospheric gravity wave response. This larger gravity wave activity is consistent with the earlier findings that the Goddard scheme produces the strongest deep convection and associated latent heating rates, which are key sources of gravity wave excitation. Among the WSM6 configurations, simulations without the Grell–3 cumulus parameterization exhibit stronger gravity wave activity than those employing Grell–3, suggesting that explicitly resolved convection in Domain 02 more effectively drives wave generation than parameterized convection. In contrast, differences among PBL schemes primarily modulate the horizontal structure and spatial distribution of the wave field rather than its magnitude, reflecting their secondary role in controlling wave generation at these altitudes.

To assess whether differences in simulated gravity wave activity are related to variations in background propagation conditions, we examined the mean horizontal wind speed and temperature profiles in the stratosphere within Domain 02 during the

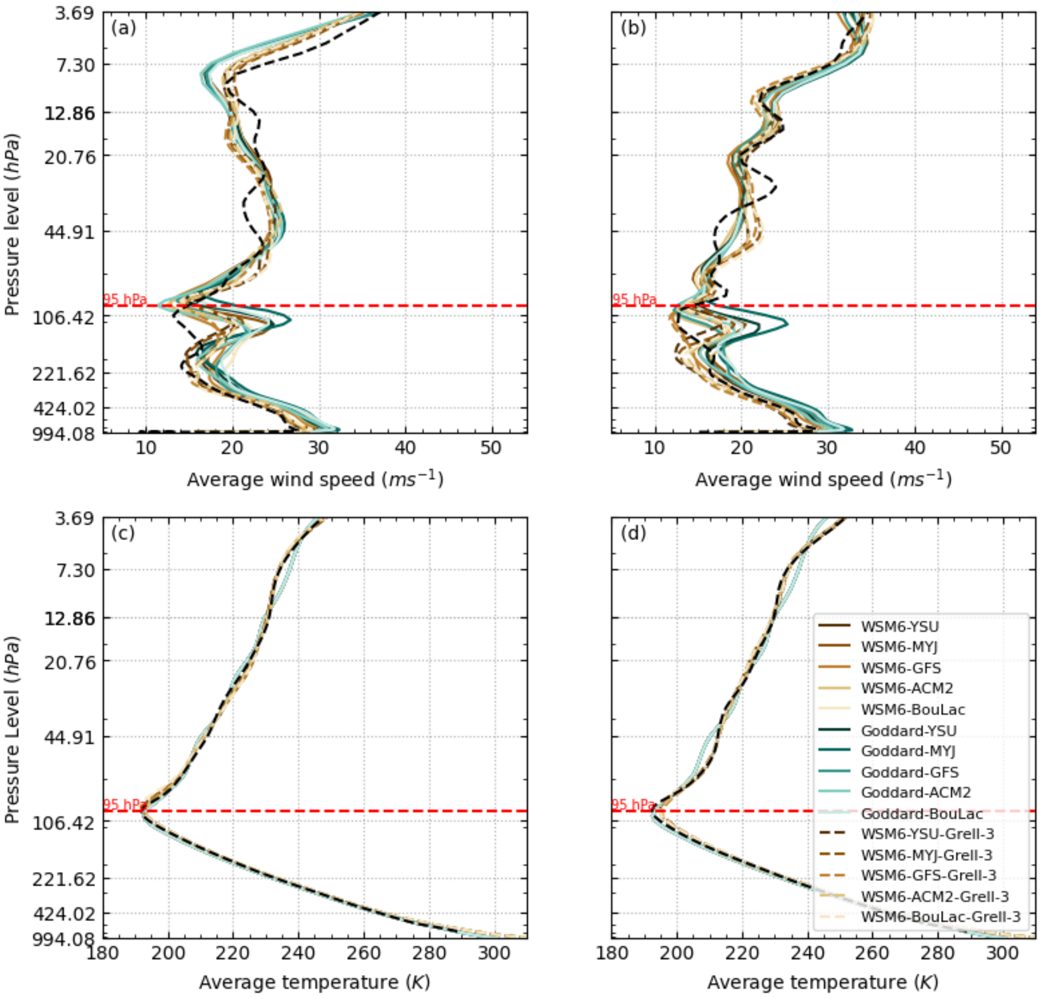

Figure 13. Mean vertical profiles of horizontal wind speed (a,b) and temperature (c,d) in Domain 02 from all WRF simulations compared with the ERA5 reanalysis (black line). Panels (a,c) correspond to +27 h and panels (b,d) to +36 h. Profiles are averaged over Domain 02 and interpolated to ERA5 vertical levels to facilitate direct comparison.

TC intensification (+27 h) and peak-intensity (+36 h) stages (Fig. 13). In the stratosphere, the simulated wind profiles exhibit some variability among physics configurations but are mostly consistent with the ERA5 reanalysis, indicating that the large-scale flow controlling gravity wave propagation is similarly represented across the simulations. The deviations of the simulated wind speeds from ERA5 are generally small, typically remaining within approximately $\pm 5\,\mathrm{m\,s^{-1}}$, while the differences among the simulations themselves are even smaller. The temperature profiles show very good agreement with ERA5 at both stages, which is expected given that ERA5 provides the initial and lateral boundary conditions for the WRF simulations. Temperature differences between the simulations and ERA5 are likewise small, generally within about $\pm 3\,\mathrm{K}$, and the simulations show an even closer agreement with each other. The relatively small differences in stratospheric wind and stability conditions suggest that variations in the background propagation environment are not the primary driver of the inter-simulation differences in gravity wave activity. Instead, these differences are mostly attributable to variations in diabatic heating structure and convective forcing.

3.6 Sensitivity of gravity wave spectra to model physics

To quantify how physics parameterizations affect gravity wave characteristics, we analyze gravity wave amplitudes and wavelengths derived from an S-transform analysis of the vertical velocity field. To focus on dynamically relevant waves and suppress noise from weak perturbations, only gravity wave components with amplitudes exceeding $0.3\,\mathrm{m\,s^{-1}}$ are retained in the spectral analysis. This threshold is motivated by the amplitude distribution (Fig. A1), which separates a large population of weak, incoherent perturbations from a smaller number of intense and spatially coherent gravity wave events. Applying this threshold therefore isolates the dominant wave packets that contribute most strongly to vertical momentum and energy transport.

Because the S-transform is applied to finite spatial domains, the estimated wave amplitude can depend to some extent on the wavelength and on the number of observable wave cycles within a wave packet. In particular, waves with vertical wavelengths approaching the depth of the analysis domain may exhibit reduced estimated amplitudes, which could increase the likelihood that such waves fall below the applied amplitude threshold (Hindley et al., 2019). This effect is expected to be small for the dominant wavelength range identified in our simulations but should nevertheless be considered when interpreting the statistics of the detected wave population.

The statistics of the gravity wave spectral parameters are summarized in Fig. 14, which shows boxplots of gravity wave amplitude, horizontal wavelength, and vertical wavelength at $20\,\mathrm{km}$ and $40\,\mathrm{km}$ altitude during the TC intensification period (+27 h), when gravity wave activity reaches its maximum in the simulations compared with the later peak-intensity stage. The median horizontal wavelength is largest for WSM6–Grell–3 and smallest for the Goddard microphysics scheme, suggesting that differences in convective organization and latent heating structure among the physics configurations influence the dominant horizontal scales of the generated gravity waves. While WSM6–Grell–3 combined with YSU produces the least variability in horizontal wavelength, the Goddard–ACM2 combination yields the least variability in vertical wavelength.

The Goddard–GFS configuration yields the largest median gravity wave amplitude of $0.48\,\mathrm{m\,s^{-1}}$ at $20\,\mathrm{km}$ during the TC intensification stage (+27 h), which is about $33\,\%$ larger than the minimum value of $0.36\,\mathrm{m\,s^{-1}}$ produced by WSM6–GFS. Regarding horizontal scales, WSM6–ACM2 produces the largest median horizontal wavelength of $45.5\,\mathrm{km}$, approximately $36\,\%$ larger than the smallest value of $33.5\,\mathrm{km}$ produced by Goddard–MYJ. For vertical scales at +27 h, WSM6–GFS yields the largest median vertical wavelength of $7.1\,\mathrm{km}$, about $55\,\%$ larger than the minimum value of $4.7\,\mathrm{km}$ produced by Goddard–MYJ. At the $20\,\mathrm{km}$ level, the ACM2 PBL scheme produces the largest spread of horizontal wavelengths ($71.8\,\mathrm{km}$), whereas the GFS PBL scheme yields the narrowest spread ($55.6\,\mathrm{km}$).

In addition to differences in median values, the physics configurations also produce notable differences in the spread of gravity wave parameters. Our results indicate that Goddard–GFS exhibits the greatest range of gravity wave amplitudes (defined by the 5th and 95th percentiles), between $0.2\,\mathrm{m\,s^{-1}}$ and $1.6\,\mathrm{m\,s^{-1}}$, whereas WSM6–MYJ produces the smallest range,

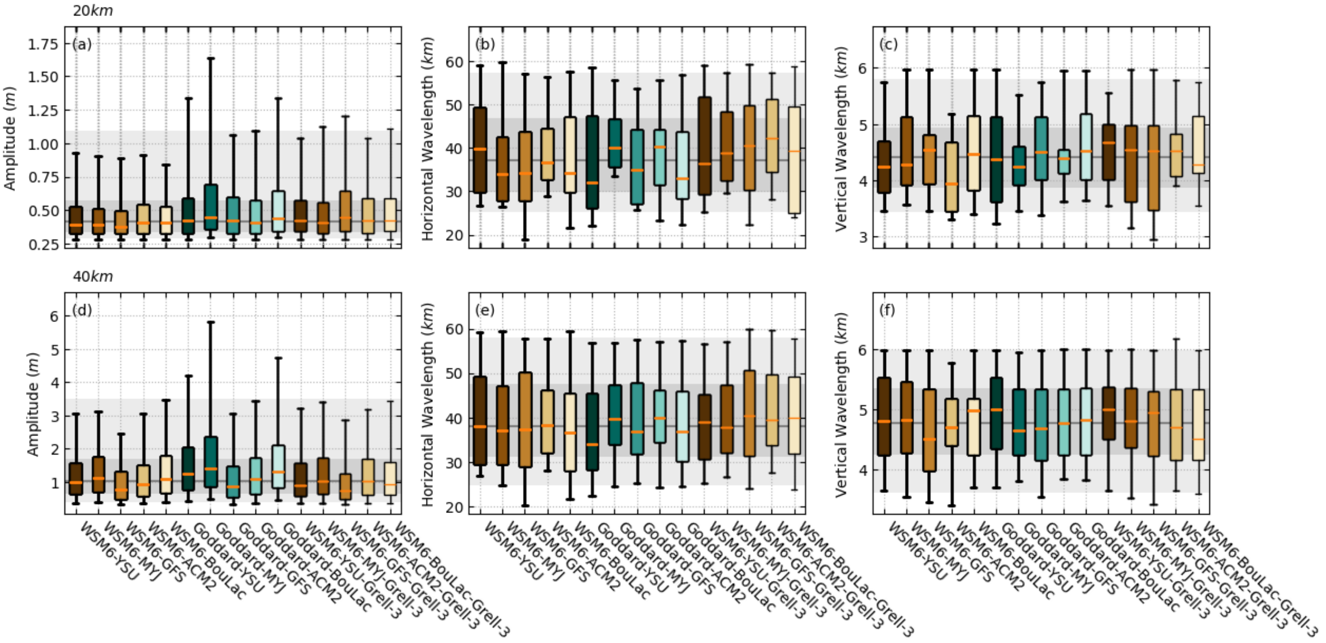

Figure 14. Distribution of gravity wave parameters during the TC intensification period (+27 h) at 20 km (a–c) and 40 km (d–f) altitude. Parameters include gravity wave amplitude (left column), horizontal wavelength (middle column), and vertical wavelength (right column), derived from S-transform analysis of the vertical velocity field. Each boxplot summarizes results from all physics configurations (microphysics, PBL, and cumulus schemes). The horizontal grey lines indicate the median across all cases. Boxes and whiskers denote the 25th–75th and 5th–95th percentiles, respectively. The dark and light grey shaded bands indicate the interquartile (25th–75th) and full (5th–95th) ranges across all simulations.

between $0.2\,\mathrm{m\,s^{-1}}$ and $0.7\,\mathrm{m\,s^{-1}}$. For horizontal wavelengths, Goddard–GFS also shows the largest range, spanning $24.0\,\mathrm{km}$ to $107.0\,\mathrm{km}$, while WSM6–YSU–Grell–3 yields the smallest range, between $3.9\,\mathrm{km}$ and $18.7\,\mathrm{km}$. For vertical wavelengths, WSM6–GFS–Grell–3 exhibits the largest range, between $2.9\,\mathrm{km}$ and $14.9\,\mathrm{km}$, whereas Goddard–ACM2 produces the smallest range, between $3.4\,\mathrm{km}$ and $10.7\,\mathrm{km}$. These results demonstrate that physics parameterizations influence not only the amplitude of TC-generated gravity waves but also their dominant horizontal and vertical scales.

4 Discussion

4.1 Context and limitations of intercomparison studies

Direct comparisons among tropical cyclone simulation studies are inherently challenging, as results depend on storm-specific characteristics, model resolution, domain configuration, initial and boundary conditions, and other factors such as the specific versions and implementations of physics parameterizations. Even when using the same numerical model, differences in horizontal resolution, nesting strategy, and simulation period can lead to substantial variability in simulated tropical cyclone (TC) structure and evolution. As summarized by Shirai et al. (2022), no single combination of microphysics and planetary boundary layer (PBL) schemes consistently outperforms others across different TC cases and modeling setups.

Our results are consistent with this broader finding. Although some physics configurations perform better for certain metrics, such as track error, TC intensity, or cloud structure, no single configuration dominates across all diagnostics. This reinforces the notion that TC simulations remain strongly case-dependent and that physics parameterizations should be selected based on the scientific question being addressed, rather than assuming a universally optimal configuration. In particular, the sensitivity of latent heating structure and gravity wave characteristics to model physics highlighted in this study illustrates how different parameterizations can influence the representation of small-scale dynamical processes in TC simulations.

This study focuses on a single, well-observed and well-studied tropical cyclone case to enable a detailed and internally consistent investigation of the links between model physics, convective heating, and gravity wave generation. Each physics configuration requires high-resolution, multi-day simulations with an extended vertical domain and high-frequency model output, followed by computationally intensive post-processing and localized spectral analysis. Extending this approach to multiple storms would require substantially greater computational resources and could limit the depth of physical interpretation achievable for each case.

By focusing on Typhoon Soudelor, which exhibits strong, well-organized convection and pronounced gravity wave signatures in satellite observations, we are able to systematically isolate the effects of microphysics, boundary layer, and cumulus parameterizations under controlled conditions. Although this single-case approach limits the generality of the quantitative results to some extent, it enables a more rigorous investigation of the physical mechanisms governing the generation of gravity waves in the stratosphere, allowing differences in wave characteristics to be attributed primarily to variations in diabatic forcing rather than to environmental variability.

4.2 Tropical cyclone structure and convection compared with previous studies

The simulated tracks of Typhoon Soudelor show close agreement with the IBTrACS best-track estimates during the early and mature stages of the storm, with track errors below 100 km prior to landfall. A systematic northward track bias after landfall is present in all simulations, consistent with earlier studies of Soudelor using the HWRF framework (Li and Huang, 2019). In contrast, Chane Ming et al. (2019) reported a slightly southward landfall bias, although their study does not document the storm track in the hours following landfall. This suggests that the post-landfall track deviation is likely related to large-scale environmental conditions and land-interaction effects, rather than to specific physics parameterizations.

Sensitivity to microphysics and PBL schemes is evident in simulated TC intensity and cloud structure. Consistent with earlier work (Yang and Lin, 2005; Choudhury and Das, 2017; Shirai et al., 2022), the choice of microphysics strongly influences convective strength and the depth of latent heating, while PBL schemes exert a primary control on storm structure and track evolution. In our simulations, the Goddard microphysics scheme tends to produce stronger and deeper convection than WSM6, in better agreement with satellite-derived cloud properties, but often at the cost of overestimating storm intensity. The inclusion of cumulus parameterization weakens resolved convection, as also reported by Yang and Lin (2005), and reduces deep convective heating, consistent with previous findings that cumulus schemes can suppress explicit convection at convection-permitting resolutions.

Improved agreement with observed TC intensity or track evolution does not necessarily imply a more realistic representation of convective structure or diabatic heating. This distinction is particularly important when evaluating model performance beyond traditional TC metrics, especially when the scientific focus extends beyond surface impacts to upper-atmospheric processes such as the generation and propagation of stratospheric gravity waves.

4.3 Implications for gravity wave generation and vertical coupling

One key result of this study is that simulations producing broadly similar TC tracks and intensity evolution can nevertheless generate significantly different stratospheric gravity wave responses. These differences are closely linked to variations in the magnitude and vertical distribution of latent heating, which are widely recognized as the primary forcing mechanism for gravity waves generated by deep convection (Beres et al., 2002; Alexander et al., 2021), including organized convective systems such as tropical cyclones (e.g., Kim et al., 2007, 2009). Because tropical cyclones consist of intense, vertically deep convection, differences in the vertical structure and altitude of diabatic heating can substantially influence the characteristics of the resulting stratospheric gravity wave field.

Across the fifteen simulations, configurations with deeper and higher-altitude heating are associated with systematically larger vertical velocity variability in the stratosphere, indicating more efficient wave forcing. This behavior is consistent with linear gravity wave theory, which shows that the vertical extent and altitude of diabatic heating strongly influence the amplitude and spectral characteristics of the resulting wave field. In particular, the vertical structure of the heating determines the vertical wavenumber of the excited waves, which can lead to larger variability in vertical wavelengths. Consistent with this theoretical expectation, our spectral analysis reveals larger variability in the vertical wavelengths of the simulated gravity waves, while horizontal wavelengths show comparatively weaker sensitivity to changes in physics configurations. These results indicate that model physics primarily control gravity wave activity by modifying the vertical structure and intermittency of diabatic heating, which in turn influences the efficiency and spectrum of wave generation. These differences may also imply substantial variations in gravity-wave momentum flux and the associated mean-flow forcing.

Microphysics schemes strongly influence the altitude of peak latent heating, with the Goddard microphysics scheme shifting the heating maximum to higher levels than WSM6. This vertical displacement of the forcing leads to systematic differences in gravity wave spectral characteristics, as revealed by diagnostics based on vertical velocity variability and S-transform spectral analysis. PBL schemes further modulate gravity wave characteristics by influencing convective organization and the spatial and temporal variability of diabatic heating, while cumulus parameterization consistently reduces the amplitudes of resolved gravity waves in the stratosphere. Together, these results highlight the strong sensitivity of stratospheric gravity wave activity to the representation of convection and diabatic heating in numerical weather prediction models.

Background wind and stability conditions are broadly similar across physics configurations, indicating that the observed differences in gravity wave spectra arise primarily from variations in convective forcing rather than from differences in wave propagation conditions. This demonstrates the strong sensitivity of gravity wave generation to the vertical structure of diabatic

https://doi.org/10.5194/egusphere-2026-1469
Preprint. Discussion started: 23 April 2026

heating and emphasizes the need for careful evaluation of convective parameterizations when using mesoscale models to study atmospheric gravity wave processes in the stratosphere.

4.4 Broader implications and outlook

These findings have important implications for studies of atmospheric vertical coupling. Gravity waves generated by tropical cyclones contribute to momentum transport and circulation changes in the stratosphere and mesosphere, yet their representation in numerical models depends strongly on the representation of physical processes in the troposphere, particularly convection and diabatic heating. Our results suggest that even when TC simulations are considered successful by conventional metrics, their gravity wave impacts may differ substantially depending on the choice of model physics parameterizations.

Future work should therefore prioritize coordinated evaluation of TC simulations against both tropospheric and upper-atmospheric observations, including direct gravity wave diagnostics. Ensemble-based modeling approaches and targeted observations could help constrain uncertainties in convective heating and improve confidence in modeled gravity wave forcing. Ultimately, improving the representation of gravity wave sources in tropical cyclones will enhance our understanding of their role in atmospheric vertical coupling and climate variability.

5 Conclusions

In this study, we examined how different physics parameterizations in the WRF model affect the simulation of Typhoon Soudelor (2015) and the associated generation of stratospheric gravity waves. A suite of simulations employing multiple microphysics, planetary boundary layer, and cumulus parameterizations was evaluated against IBTrACS best-track estimates and satellite observations, with gravity wave diagnostics derived from the vertical velocity field. The simulated tropical cyclone tracks and intensities show good agreement with observations during the early and mature stages of the storm, with differences among physics configurations remaining within observational uncertainty prior to landfall.

Despite this similarity in large-scale tropical cyclone evolution, substantial sensitivity is evident in the simulated convective structure, latent heating, and gravity wave response. Variations in microphysics and boundary layer schemes lead to systematic differences in the magnitude and vertical distribution of latent heating, which in turn strongly influence gravity wave amplitudes and spectral characteristics in the stratosphere. The inclusion of cumulus parameterization in the outer model domain consistently weakens resolved convection and reduces gravity wave amplitudes.

The Goddard–GFS configuration yields the largest median gravity wave amplitude at the $20\,\mathrm{km}$ level during the TC intensification stage, about $33\,\%$ larger than the minimum produced by WSM6–GFS. Regarding horizontal scales, WSM6–ACM2 produces the largest median horizontal wavelength, approximately $36\,\%$ larger than the smallest value produced by Goddard–MYJ. WSM6–GFS yields a median vertical wavelength about $55\,\%$ larger than the minimum produced by Goddard–MYJ. The ACM2 PBL scheme produces the largest range of horizontal wavelengths ($71.8\,\mathrm{km}$), while the GFS PBL scheme yields the narrowest range ($55.6\,\mathrm{km}$).

https://doi.org/10.5194/egusphere-2026-1469
Preprint. Discussion started: 23 April 2026

These differences arise despite comparable background wind and stability conditions, indicating that the simulated gravity wave response is primarily driven by differences in diabatic forcing rather than variations in wave propagation conditions. Our results demonstrate that, for the case of Typhoon Soudelor, tropical cyclone simulations that appear similar according to conventional metrics can nevertheless produce significantly different gravity wave responses, underscoring the strong sensitivity of wave generation to model physics parameterizations.

While this study is limited to a single, well-observed storm, it provides a detailed process-oriented assessment of how physical parameterizations influence convective heating and gravity wave generation. The analysis framework presented here offers a foundation for future multi-case studies aimed at assessing the generality of these sensitivities across a broader range of tropical cyclone environments.

Code and data availability. The Weather Research and Forecasting (WRF) model is publicly available from the National Center for Atmospheric Research (NCAR) at https://www2.mmm.ucar.edu/wrf/users/. The scripts used to generate the WRF namelists and preprocessing inputs for this study are available from the GitHub repository at https://github.com/hydrogencl/WRF_TOOLS. The International Best Track Archive for Climate Stewardship (IBTrACS) tropical cyclone data (Knapp et al., 2010) are available at the NOAA National Centers for Environmental Information at https://www.ncei.noaa.gov/products/international-best-track-archive. The FY-2G outgoing longwave radiation (OLR) data are available from the National Satellite Meteorological Center (NSMC) at http://satellite.nsmc.org.cn (NSMC, 2025). The AIRS gravity wave data sets (Hoffmann, 2021) are available at https://datapub.fz-juelich.de/slcs/airs/gravity_waves. ERA5 reanalysis data (Hersbach et al., 2020), used for initial and boundary conditions, are produced by the European Centre for Medium-Range Weather Forecasts and can be accessed through the Copernicus Climate Data Store at https://cds.climate.copernicus.eu.

Appendix A: Sensitivity of gravity wave detection to amplitude threshold

A sensitivity analysis was conducted to evaluate how the choice of amplitude threshold affects the spatial coverage of detected gravity wave signals at $20\,\mathrm{km}$ altitude. The coverage is defined as the fraction of grid points within the analysis domain where the gravity wave amplitude exceeds a specified threshold derived from the S-transform wave spectra. Table A1 summarizes the ranges of coverage across all physics configurations for several amplitude thresholds during the intensification (+27 h) and peak (+36 h) stages of the storm. As expected, lower thresholds yield substantially larger spatial coverage, whereas higher thresholds progressively isolate the most intense gravity wave events.

For a threshold of $0.3\,\mathrm{m\,s^{-1}}$, the spatial coverage ranges from 12.7% to 50.2% during the intensification stage (+27 h) and from 9.4% to 44.7% during the peak stage (+36 h). This threshold provides a suitable balance between retaining dynamically relevant gravity wave signals and excluding weak perturbations that are likely associated with background variability or noise. Figure A1 illustrates the spatial distribution of gravity wave amplitudes after applying the $0.3\,\mathrm{m\,s^{-1}}$ threshold at +36 h. The remaining signals are primarily concentrated near the inner core and along the outer periphery of the tropical cyclone, consistent with regions of strong convective forcing and associated gravity wave generation.

Table A1. Ranges of spatial coverage of gravity wave signals exceeding different amplitude thresholds at 20 km altitude during the intensification (+27 h) and peak (+36 h) stages of the storm.

Threshold (m s^{-1})	+27 h	+36 h
0.1	64.6%–97.6%	57.6%–96.7%
0.2	27.5%–76.8%	22.7%–70.1%
0.3	12.7%–50.2%	9.4%–44.7%
0.4	6.2%–33.6%	4.0%–30.9%
0.5	3.4%–23.9%	1.6%–21.8%

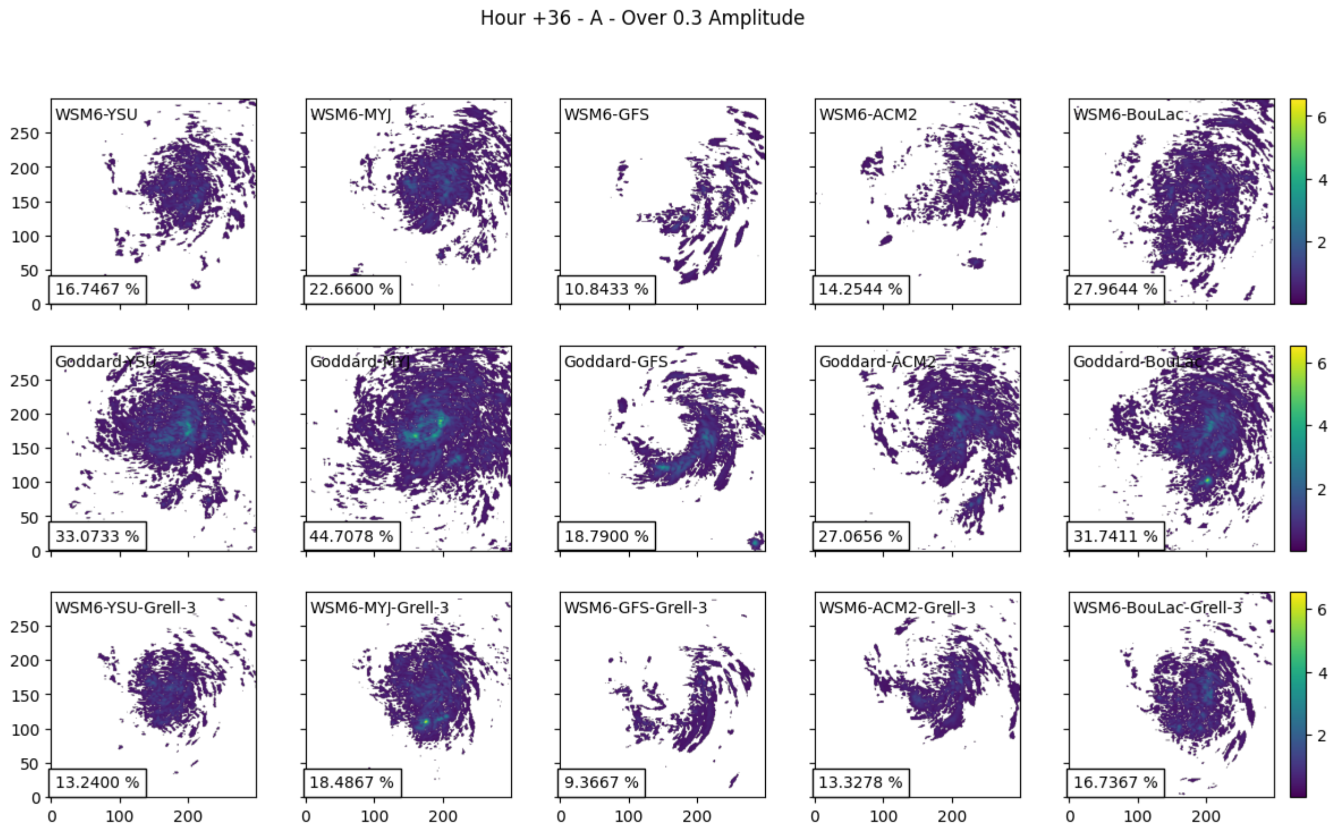

Figure A1. Spatial distribution of gravity wave amplitudes derived from the S-transform analysis at 20 km altitude at +36 h after applying an amplitude threshold of $0.3\,\mathrm{m\,s^{-1}}$. Only wave components exceeding this threshold are shown, highlighting regions of strongest gravity wave activity near the tropical cyclone.

Author contributions. YSL conducted the WRF simulations and analyzed the results. XW performed the latent heating rate analysis and provided the FengYun-2G OLR data. CJW developed and applied the S-transform analysis. NPH led the development of the S-transform analysis code. LH provided the AIRS gravity wave observations. All authors contributed to the study design and to writing and revising the manuscript.

Competing interests. The authors declare that they have no competing interests.

Financial support. XW was funded by the National Natural Science Foundation of China (grant nos. 42475068 and W2521143), the National Major Science and Technology Projects (grant no. 2025ZD1204803), and the Strategic Priority Research Program of the Chinese Academy of Sciences (grant no. XDB0760101). CJW was supported by NERC grants NE/S00985X/1, NE/V01837X/1, NE/W003201/1, and NE/Z50399X/1, the Royal Society University Research Fellowship URF/R/221023, and the Leverhulme Trust Research Project Grant RPG-2025-467. NPH is funded by UK Natural Environment Research Council awards NE/X017842/1, NE/Z50399X/1, and NE/W003201/1.

Acknowledgements. The authors gratefully acknowledge the Gauss Centre for Supercomputing e.V. for funding this project by providing computing time through the John von Neumann Institute for Computing (NIC) on the GCS Supercomputer JUWELS at Jülich Supercomputing Centre (JSC). We thank Olaf Stein for helpful comments and feedback on an earlier draft of this manuscript.

References

Alexander, M. J., Holton, J. R., and Durran, D. R.: The gravity-wave response above deep convection in a squall line simulation, Journal of the Atmospheric Sciences, 52, 2212–2226, https://doi.org/10.1175/1520-0469(1995)052<2212:TGWRAD>2.0.CO;2, 1995.

Alexander, M. J., Liu, C. C., Bacmeister, J., Bramberger, M., Hertzog, A., and Richter, J. H.: Observational Validation of Parameterized Gravity Waves From Tropical Convection in the Whole Atmosphere Community Climate Model, Journal of Geophysical Research: Atmospheres, 126, e2020JD033 954, https://doi.org/10.1029/2020JD033954, 2021.

Aumann, H., Chahine, M., Gautier, C., Goldberg, M., Kalnay, E., McMillin, L., Revercomb, H., Rosenkranz, P., Smith, W., Staelin, D., Strow, L., and Susskind, J.: AIRS/AMSU/HSB on the Aqua mission: design, science objectives, data products, and processing systems, IEEE Transactions on Geoscience and Remote Sensing, 41, 253–264, https://doi.org/10.1109/TGRS.2002.808356, 2003.

Beres, J. H., Alexander, M. J., and Holton, J. R.: Effects of Tropospheric Wind Shear on the Spectrum of Convectively Generated Gravity Waves, Journal of the Atmospheric Sciences, 59, 1805–1824, https://doi.org/10.1175/1520-0469(2002)059<1805:EOTWSO>2.0.CO;2, 2002.

Cangialosi, J. P., Blake, E., DeMaria, M., Penny, A., Latto, A., Rappaport, E., and Tallapragada, V.: Recent Progress in Tropical Cyclone Intensity Forecasting at the National Hurricane Center, Weather and Forecasting, 35, 1913–1922, https://journals.ametsoc.org/view/journals/wefo/35/5/wafD200059.xml, 2020.

Chahine, M. T., Pagano, T. S., Aumann, H. H., Atlas, R., Barnet, C., Blaisdell, J., Chen, L., Divakarla, M., Fetzer, E. J., Goldberg, M., Gautier, C., Granger, S., Hannon, S., Irion, F. W., Kakar, R., Kalnay, E., Lambrigtsen, B. H., Lee, S.-Y., Marshall, J. L., McMillan, W. W., McMillin, L., Olsen, E. T., Revercomb, H., Rosenkranz, P., Smith, W. L., Staelin, D., Strow, L. L., Susskind, J., Tobin, D., Wolf, W., and Zhou, L.: AIRS: Improving Weather Forecasting and Providing New Data on Greenhouse Gases, Bulletin of the American Meteorological Society, 87, 911–926, https://doi.org/10.1175/BAMS-87-7-911, 2006.

Chane Ming, F., Jolivet, S., Liou, Y.-A., Jégou, F., Mekies, D., and Hong, J.-S.: Elliptical Structures of Gravity Waves Produced by Typhoon Soudelor in 2015 near Taiwan, Atmosphere, 10, https://doi.org/10.3390/atmos10050260, 2019.

Chen, J.-H., Lin, S.-J., Magnusson, L., Bender, M., Chen, X., Zhou, L., Xiang, B., Rees, S., Morin, M., and Harris, L.: Advancements in Hurricane Prediction With NOAA's Next-Generation Forecast System, Geophysical Research Letters, 46, 4495–4501, https://doi.org/10.1029/2019GL082410, 2019.

Choudhury, D. and Das, S.: The sensitivity to the microphysical schemes on the skill of forecasting the track and intensity of tropical cyclones using WRF-ARW model, Journal of Earth System Science, 126, 57, https://doi.org/10.1007/s12040-017-0830-2, 2017.

Chu, K., Xiao, Q., Tan, Z.-m., and Gu, J.: A forecast sensitivity study on the intensity change of Typhoon Sinlaku (2008), J. Geophys. Res., 116, https://doi.org/https://doi.org/10.1029/2011JD016127, 2011.

Davis, C., Wang, W., Chen, S. S., Chen, Y., Corbosiero, K., DeMaria, M., Dudhia, J., Holland, G., Klemp, J., Michalakes, J., Reeves, H., Rotunno, R., Snyder, C., and Xiao, Q.: Prediction of Landfalling Hurricanes with the Advanced Hurricane WRF Model, Monthly Weather Review, 136, 1990 – 2005, https://doi.org/10.1175/2007MWR2085.1, 2008.

DeMaria, M., Sampson, C. R., Knaff, J. A., and Musgrave, K. D.: Is Tropical Cyclone Intensity Guidance Improving?, Bulletin of the American Meteorological Society, 95, 387–398, https://journals.ametsoc.org/view/journals/bams/95/3/bams-d-12-00240.1.xml, 2014.

Emanuel, K. and Zhang, F.: On the Predictability and Error Sources of Tropical Cyclone Intensity Forecasts, Journal of the Atmospheric Sciences, 73, 3739 – 3747, https://doi.org/10.1175/JAS-D-16-0100.1, 2016.

Emanuel, K. A.: Increasing destructiveness of tropical cyclones over the past 30 years, Nature, 436, 686–688, https://doi.org/10.1038/nature03906, 2005.

Fakour, H., Lo, S.-L., and Lin, T.-F.: Impacts of Typhoon Soudelor (2015) on the water quality of Taipei, Taiwan, Scientific Reports, 6, 25 228, https://doi.org/10.1038/srep25228, 2016.

Gentry, M. S. and Lackmann, G. M.: Sensitivity of Simulated Tropical Cyclone Structure and Intensity to Horizontal Resolution, Monthly Weather Review, 138, 688 – 704, https://doi.org/10.1175/2009MWR2976.1, 2010.

Gettelman, A., Geer, A. J., Forbes, R. M., Carmichael, G. R., Feingold, G., Posselt, D. J., Stephens, G. L., van den Heever, S. C., Varble, A. C., and Zuidema, P.: The future of Earth system prediction: Advances in model-data fusion, Science Advances, 8, eabn3488, https://doi.org/10.1126/sciadv.abn3488, 2022.

Hersbach, H., Bell, B., Berrisford, P., Hirahara, S., Horányi, A., Muñoz-Sabater, J., Nicolas, J., Peubey, C., Radu, R., Schepers, D., Simmons, A., Soci, C., Abdalla, S., Abellan, X., Balsamo, G., Bechtold, P., Biavati, G., Bidlot, J., Bonavita, M., De Chiara, G., Dahlgren, P., Dee, D., Diamantakis, M., Dragani, R., Flemming, J., Forbes, R., Fuentes, M., Geer, A., Haimberger, L., Healy, S., Hogan, R. J., Hólm, E., Janisková, M., Keeley, S., Laloyaux, P., Lopez, P., Lupu, C., Radnoti, G., de Rosnay, P., Rozum, I., Vamborg, F., Villaume, S., and Thépaut, J.-N.: The ERA5 global reanalysis, Quarterly Journal of the Royal Meteorological Society, 146, 1999–2049, https://doi.org/10.1002/qj.3803, 2020.

Hindley, N. P., Smith, N. D., Wright, C. J., Rees, D. A. S., and Mitchell, N. J.: A two-dimensional Stockwell transform for gravity wave analysis of AIRS measurements, Atmospheric Measurement Techniques, 9, 2545–2565, https://doi.org/10.5194/amt-9-2545-2016, 2016.

Hindley, N. P., Wright, C. J., Smith, N. D., Hoffmann, L., Holt, L. A., Alexander, M. J., Moffat-Griffin, T., and Mitchell, N. J.: Gravity waves in the winter stratosphere over the Southern Ocean: high-resolution satellite observations and 3-D spectral analysis, Atmospheric Chemistry and Physics, 19, 15 377–15 414, https://doi.org/10.5194/acp-19-15377-2019, 2019.

Hoffmann, L.: AIRS/Aqua Observations of Gravity Waves, https://doi.org/10.26165/JUELICH-DATA/LQAAJA, 2021.

Hoffmann, L., Xue, X., and Alexander, M. J.: A global view of stratospheric gravity wave hotspots located with Atmospheric Infrared Sounder observations, Journal of Geophysical Research: Atmospheres, 118, 416–434, https://doi.org/10.1029/2012JD018658, 2013.

Hoffmann, L., Alexander, M. J., Clerbaux, C., Grimsdell, A. W., Meyer, C. I., Rößler, T., and Tournier, B.: Intercomparison of stratospheric gravity wave observations with AIRS and IASI, Atmospheric Measurement Techniques, 7, 4517–4537, https://doi.org/10.5194/amt-7-4517-2014, 2014.

Hoffmann, L., Wu, X., and Alexander, M. J.: Satellite Observations of Stratospheric Gravity Waves Associated With the Intensification of Tropical Cyclones, Geophys. Res. Lett., 45, 1692–1700, https://doi.org/10.1002/2017GL076123, 2018.

Huang, W.-K. and Wang, J.-J.: Typhoon damage assessment model and analysis in Taiwan, Natural Hazards, 79, 497–510, https://doi.org/10.1007/s11069-015-1858-8, 2015.

Islam, M. R. and Takagi, H.: Typhoon parameter sensitivity of storm surge in the semi-enclosed Tokyo Bay, Frontiers of Earth Science, 14, 553–567, https://doi.org/10.1007/s11707-020-0817-1, 2020.

JMA: Annual Report on the Activities of the RSMC Tokyo – Typhoon Center 2015, Tech. rep., Japan Meteorological Agency, Tokyo, Japan, https://www.jma.go.jp/jma/jma-eng/jma-center/rsmc-hp-pub-eg/AnnualReport/2015/Text/Text2015.pdf, 2016.

Kim, S.-Y. and Chun, H.-Y.: Stratospheric Gravity Waves Generated by Typhoon Saomai (2006): Numerical Modeling in a Moving Frame Following the Typhoon, Journal of the Atmospheric Sciences, 67, 3617 – 3636, https://doi.org/10.1175/2010JAS3374.1, 2010.

Kim, S.-Y., Chun, H.-Y., and Baik, J.-J.: Sensitivity of typhoon-induced gravity waves to cumulus parameterizations, Geophysical Research Letters, 34, https://doi.org/10.1029/2007GL030592, 2007.

Kim, S.-Y., Chun, H.-Y., and Wu, D. L.: A study on stratospheric gravity waves generated by Typhoon Ewiniar: Numerical simulations and satellite observations, Journal of Geophysical Research: Atmospheres, 114, https://doi.org/https://doi.org/10.1029/2009JD011971, 2009.

Knapp, K. R., Kruk, M. C., Levinson, D. H., Diamond, H. J., and Neumann, C. J.: The International Best Track Archive for Climate Stewardship (IBTrACS): Unifying Tropical Cyclone Data, Bulletin of the American Meteorological Society, 91, 363–376, https://journals.ametsoc.org/view/journals/bams/91/3/2009bams2755_1.xml, 2010.

Knutson, T., Camargo, S. J., Chan, J. C. L., Emanuel, K., Ho, C.-H., Kossin, J., Mohapatra, M., Satoh, M., Sugi, M., Walsh, K., and Wu, L.: Tropical cyclones and climate change assessment part II: Projected response to anthropogenic warming, Bulletin of the American Meteorological Society, 101, E303–E322, https://doi.org/10.1175/BAMS-D-18-0194.1, 2020.

Krishnamurti, T., Pattnaik, S., Biswas, M. K., Bensman, E., Kramer, M., Surgi, N., and Kumar, T. S. V. V.: Hurricane Forecasts with a Mesoscale Suite of Models, Tellus A: Dynamic Meteorology and Oceanography, 62, 633–646, https://doi.org/10.1111/j.1600-0870.2010.00469.x, 2010.

Kruse, C. G., Alexander, M. J., Hoffmann, L., van Niekerk, A., Polichtchouk, I., Bacmeister, J. T., Holt, L., Plougonven, R., Šácha, P., Wright, C., Sato, K., Shibuya, R., Gisinger, S., Ern, M., Meyer, C. I., and Stein, O.: Observed and Modeled Mountain Waves from the Surface to the Mesosphere near the Drake Passage, Journal of the Atmospheric Sciences, 79, 909–932, https://journals.ametsoc.org/view/journals/atsc/79/4/JAS-D-21-0252.1.xml, 2022.

Lane, T. P., Reeder, M. J., and Clark, T. L.: Numerical Modeling of Gravity Wave Generation by Deep Tropical Convection, Journal of the Atmospheric Sciences, 58, 1249 – 1274, https://doi.org/10.1175/1520-0469(2001)058<1249:NMOGWG>2.0.CO;2, 2001.

Li, D.-Y. and Huang, C.-Y.: The influences of ocean on intensity of Typhoon Soudelor (2015) as revealed by coupled modeling, Atmos Sci Lett, 20, e871, https://doi.org/10.1002/asl.871, 2019.

Lu, Y.-S., Good, G. H., and Elbern, H.: Optimization of weather forecasting for cloud cover over the European domain using the meteorological component of the Ensemble for Stochastic Integration of Atmospheric Simulations version 1.0, GMD, 16, 1083–1104, https://doi.org/10.5194/gmd-16-1083-2023, 2023.

Nolan, D. S., Zhang, J. A., and Stern, D. P.: Evaluation of Planetary Boundary Layer Parameterizations in Tropical Cyclones by Comparison of In Situ Observations and High-Resolution Simulations of Hurricane Isabel (2003). Part I: Initialization, Maximum Winds, and the Outer-Core Boundary Layer, Monthly Weather Review, 137, 3651 – 3674, https://doi.org/10.1175/2009MWR2785.1, 2009.

NSMC: FY-2G data, availableat:https://satellite.nsmc.org.cn/DataPortal/cn/home/index.html, last access: 26 May 2025, 2025.

Peduzzi, P., Chatenoux, B., Dao, H., De Bono, A., Herold, C., Kossin, J., Mouton, F., and Nordbeck, O.: Global trends in tropical cyclone risk, Nature Climate Change, 2, 289–294, https://doi.org/10.1038/nclimate1410, 2012.

Richter, J. H., Sassi, F., and Garcia, R. R.: Toward a Physically Based Gravity Wave Source Parameterization in a General Circulation Model, Journal of the Atmospheric Sciences, 67, 136 – 156, https://doi.org/10.1175/2009JAS3112.1, 2010.

Satoh, M., Stevens, B., Judt, F., Khairoutdinov, M., Lin, S.-J., Putman, W. M., and Düben, P.: Global Cloud-Resolving Models, Current Climate Change Reports, 5, 172–184, https://doi.org/10.1007/s40641-019-00131-0, 2019.

Shirai, T., Enomoto, Y., Watanabe, M., and Arikawa, T.: Sensitivity analysis of the physics options in the Weather Research and Forecasting model for typhoon forecasting in Japan and its impacts on storm surge simulations, Coastal Engineering Journal, 64, 506–532, https://doi.org/10.1080/21664250.2022.2124040, 2022.

Sizemore, M., Eroglu, O., muchojp, Kinoshita, B. P., Honnorat, M., Gámez, P., Hilboll, A., Chen, H., Rowe, I., Riechert, M., Sun, S., Bonenfant, B., sfalmo, Kasprzyk, P., and dmey: NCAR/wrf-python: v1.3.4.1, https://doi.org/10.5281/zenodo.6685115, 2022.

Skamarock, W. C. and Klemp, J. B.: A time-split nonhydrostatic atmospheric model for weather research and forecasting applications, Journal of Computational Physics, 227, 3465–3485, https://doi.org/https://doi.org/10.1016/j.jcp.2007.01.037, predicting weather, climate and extreme events, 2008.

Skamarock, W. C., Klemp, J. B., Dudhia, J., Gill, D. O., Liu, Z., Berner, J., Wang, W., Powers, J. G., Duda, M. G., Barker, D. M., et al.: A description of the advanced research WRF model version 4, National Center for Atmospheric Research: Boulder, CO, USA, 145, 550, 2019.

Tao, W.-K., Shi, J. J., Chen, S. S., Lang, S., Lin, P.-L., Hong, S.-Y., Peters-Lidard, C., and Hou, A.: The impact of microphysical schemes on hurricane intensity and track, Asia-Pacific Journal of Atmospheric Sciences, 47, 1–16, https://doi.org/10.1007/s13143-011-1001-z, 2011.

Wang, C.-C., Chen, S.-H., Chen, Y.-H., Kuo, H.-C., Ruppert, J. H., and Tsuboki, K.: Cloud-resolving time-lagged rainfall ensemble forecasts for typhoons in Taiwan: Examples of Saola (2012), Soulik (2013), and Soudelor (2015), Weather and Climate Extremes, 40, 100 555, https://doi.org/10.1016/j.wace.2023.100555, 2023.

Wright, C. J.: Quantifying the global impact of tropical cyclone-associated gravity waves using HIRDLS, MLS, SABER and IBTrACS data, Quarterly Journal of the Royal Meteorological Society, 145, 3023–3039, https://doi.org/10.1002/qj.3602, 2019.

Wright, C. J., Hindley, N. P., Hoffmann, L., Alexander, M. J., and Mitchell, N. J.: Exploring gravity wave characteristics in 3-D using a novel S-transform technique: AIRS/Aqua measurements over the Southern Andes and Drake Passage, Atmospheric Chemistry and Physics, 17, 8553–8575, https://doi.org/10.5194/acp-17-8553-2017, 2017.

Wu, C.-C. and Kuo, Y.-H.: Typhoons Affecting Taiwan: Current Understanding and Future Challenges, Bulletin of the American Meteorological Society, 80, 67 – 80, https://doi.org/10.1175/1520-0477(1999)080<0067:TATCUA>2.0.CO;2, 1999.

Wu, X., Hoffmann, L., Wright, C. J., Hindley, N. P., Kalisch, S., Alexander, M. J., and Wang, Y.: Stratospheric Gravity Waves as a Proxy for Hurricane Intensification: A Case Study of Weather Research and Forecast Simulation for Hurricane Joaquin, Geophys Res Lett, 49, e2021GL097 010, https://doi.org/10.1029/2021GL097010, 2022.

Wu, X., Hoffmann, L., Wright, C. J., Hindley, N. P., Alexander, M. J., Wang, X., Chen, B., Wang, Y., and Li, M.: Mechanisms Linking Stratospheric Gravity Wave Activity to Hurricane Intensification: Insights From Model Simulation of Hurricane Joaquin, Geophysical Research Letters, 52, e2024GL113 531, https://doi.org/10.1029/2024GL113531, e2024GL113531 2024GL113531, 2025.

Xian, D., Zhang, P., Gao, L., Sun, R. J., Zhang, H. Z., and Jia, X.: Fengyun Meteorological Satellite Products for Earth System Science Applications, https://doi.org/10.1007/s00376-021-0425-3, 2021.

Yang, M.-J. and Lin, C.: A modeling study of Typhoon Toraji (2001): Physical parameterization sensitivity and topographic effect, TAO: Terrestrial, Atmospheric and Oceanic Sciences, 16, 177, https://doi.org/10.3319/TAO.2005.16.1.177(A), 2005.